

# Channel cross-section heterogeneity of particulate organic carbon transport in the Huanghe

Yutian Ke<sup>1†</sup>, Damien Calmels<sup>1</sup>, Julien Bouchez<sup>2</sup>, Marc Massault<sup>1</sup>, Benjamin Chetelat<sup>3</sup>, Aurélie Noret<sup>1</sup>, Hongming Cai<sup>2</sup>, Jiubin Chen<sup>3</sup>, Jérôme Gaillardet<sup>2</sup>, Cécile Quantin<sup>1</sup>

<sup>1</sup>GEOPS, Université Paris-Saclay-CNRS, 91405 Orsay, France

<sup>2</sup>Université de Paris, Institut de Physique du Globe de Paris, CNRS, 75005 Paris, France

<sup>3</sup>School of Earth System Science, Institute of Surface-Earth System Science, Tianjin University, 300072 Tianjin, China

<sup>†</sup>Present address: Division of Geological and Planetary Science, California Institute of Technology, Pasadena, CA 91125, USA

*Corresponding author:* Yutian Ke (yutianke@caltech.edu)

**Abstract.** The Huanghe (Yellow River), one of the largest turbid river systems in the world, has long been recognized as a major contributor of suspended particulate matter (SPM) to the ocean. However, over the last few decades, the SPM export flux of the Huanghe has decreased over 90% due to the high management, impacting the global export of particulate organic carbon (POC). To better constrain sources and modes of transport of POC beyond the previously investigated transportation of POC near the channel surface, SPM samples were for the first time collected over a whole channel cross-section in the lower Huanghe. Riverine SPM samples were analyzed for particle size and major element contents, as well as for POC content and dual carbon isotopes (<sup>13</sup>C and <sup>14</sup>C). Clear vertical and lateral heterogeneities of the physical and chemical properties of SPM are observed within the river cross-section. For instance, finer SPM carry in general more POC with higher <sup>14</sup>C activity near the surface of the right bank. Notably, we discuss how bank erosion in the alluvial plain is likely to generate lateral heterogeneity in POC composition. The Huanghe POC is millennial-aged ( $4,020 \pm 500$  radiocarbon years), dominated by organic carbon (OC) from the biosphere, while the lithospheric fraction is ca. 12%. The mobilization of aged and refractory OC, including radiocarbon-dead biospheric OC, from deeper soil horizons of the loess-paleosol sequence through erosion in the Chinese Loess Plateau is an important mechanism contributing to fluvial POC in the Huanghe drainage basin. Altogether, anthropogenic activities can drastically change the compositions and transport dynamics of fluvial POC, consequentially altering the feedback of the source-to-sink trajectory of a river system to regional and global carbon cycles.

## 29 **1 Introduction**

30 Rivers are the main conveyor of rock and soil debris eroded from the continents to the ocean. Along with inorganic  
31 material, river sediments host particulate organic carbon (POC) derived mainly from three major sources: 1) recently  
32 photosynthesized OC of the biosphere, 2) aged and altered OC from soils, and 3) ancient OC contained in sedimentary  
33 rocks (Blair et al., 2010). The net effect of riverine POC transport on the carbon cycle and thus on the evolution of  
34 Earth's climate depends on POC provenance and fate. The effective sedimentary burial of POC derived from the  
35 terrestrial biosphere (biospheric OC,  $OC_{bio}$ ) represents a net, long-term sink of atmospheric  $CO_2$  (Galy et al., 2007,  
36 Bouchez et al., 2014; Hilton et al., 2015), whereas the oxidation of POC derived from continental rocks (petrogenic  
37 OC,  $OC_{petro}$ ) acts as a net, long-term source of  $CO_2$  to the atmosphere (Hilton et al., 2014). The erosion and burial of  
38  $OC_{petro}$  escaping from oxidation has no net effect on the long-term carbon cycle (Galy et al., 2008a; Bouchez et al.,  
39 2010; Hilton et al., 2011; Horan et al., 2019). In addition, the reactive nature of  $OC_{bio}$  might also result in short-term  
40  $CO_2$  emission during transport from both river channels and recently-deposited sediments (Mayorga et al., 2005; Galy  
41 and Eglinton, 2011; Blair and Aller, 2012).

42 Globally, rivers transport a total POC flux of *ca.* 200 Tg C/year, consisting of  $157^{+74}_{-50}$  Tg C/year of  $OC_{bio}$  and  $43^{+61}_{-25}$   
43 Tg C/year of  $OC_{petro}$  (Galy et al., 2015; Ludwig et al., 1996). Source-to-sink processes controlling the origin and fate  
44 of riverine POC are prominently river-specific, suggesting that the impact of POC on regional and global carbon  
45 cycles might significantly vary both spatially and temporally (Blair and Aller, 2012). It is thus crucial to understand  
46 the mechanisms controlling the POC export by large rivers that integrate vast portions of the land surface, and quantify  
47 the differing sources of carbon exported by those large river systems.

48 The Huanghe (Yellow River) is a highly turbid river system that exports over 85% of its OC as particulate matter,  
49 with efficient deposition and preservation in the ocean (Cauwet and Mackenzie, 1993; Bianchi, 2011; Zhang et al.,  
50 2013; Ran et al., 2013). The Huanghe has been highly managed over the last few decades through water and soil  
51 conservation measures as well as reservoir construction, leading to a decrease of nearly 90% of its sediment load  
52 (Wang and Fu et al., 2016; Wang et al., 2007; Milliman et al., 1987) and a significant decrease in its POC delivery to  
53 the ocean (Zhang et al., 2013). Reservoir construction dramatically affects the transport and fate of both sediment load  
54 and POC in large rivers (Syvitski et al., 2005; Li et al., 2015). The estimated POC flux of the Huanghe is thought to  
55 have shifted from 4.5 Tg C/yr in the 1980s (Cauwet and Mackenzie, 1993) to 0.34-0.58 Tg C/yr nowadays (Tao et al.,  
56 2018) in response to both anthropogenic influence (Hu et al., 2015; Tao et al., 2018; Yu et al., 2019a) and natural  
57 variability of the regional hydrological cycle (Qu et al., 2020). These large-scale perturbations have likely modified  
58 the OC input from the different terrestrial pools as well as the fate of exported POC that was previously reaching  
59 deposition centers in the ocean and that now remains stuck on land. Those alterations of the carbon cycle remain to  
60 be addressed.

61 Over the last decade, POC transport in the Huanghe has been investigated for 1) determination and quantification of  
62 POC sources, based on bulk or molecular carbon isotopic composition (Tao et al., 2015; Yu et al., 2019b; Ge et al.,  
63 2020; Qu et al., 2020); 2) temporal and spatial variations in POC export and distribution among different size fractions  
64 (Ran et al., 2013; Wang 2012; 2016; Yu et al., 2019a, b ; Qu et al., 2020); 3) impact of anthropogenic activities (Hu

65 et al., 2015; Tao et al., 2018; Yu et al., 2019a); and 4) burial efficiency and preservation in the ocean (Sun et al., 2018;  
66 Tao et al., 2016; Ge et al., 2020). However, all these previous studies rely on suspended sediment samples collected  
67 near the channel surface or at a single, intermediate depth in the river channel, further assuming a homogeneous  
68 distribution of suspended sediment characteristics in the water column, both vertically and laterally. It is now well  
69 recognized that suspended sediments present physical, mineralogical, chemical, and isotopic heterogeneities across  
70 river transect due to hydrodynamic sorting and tributary mixing (Galy et al., 2008b; Garzanti et al., 2010; Bouchez et  
71 al., 2010, 2011a). This is also true for POC, whose age and composition vary following vertical water depth (e.g.,  
72 Galy et al., 2008b; Bouchez et al., 2014; Hilton et al., 2015; Repasch et al., 2021; Schwab et al., 2022), and lateral  
73 river transect (e.g., Bouchez et al., 2014; Baronas et al., 2020), and between sediment size fractions separated in the  
74 laboratory (Yu et al., 2019b; Ge et al., 2020). Such heterogeneity warrants a re-evaluation of POC transport in the  
75 Huanghe, accounting for the variability in suspended sediment characteristics over the channel cross-section.  
76 In this study, we take advantage of in-river hydrodynamic sorting to access the full range of suspended sediment size  
77 fractions by collecting suspended particulate matter (SPM) samples along several river depth profiles distributed  
78 across a channel transect (e.g., Bouchez et al., 2014; Freymond et al., 2018; Baronas et al., 2020). We apply this  
79 sampling scheme to a cross-section of the Huanghe located 200 km upstream from the river mouth and report SPM  
80 OC content, stable isotope composition, and radiocarbon activity as well as total nitrogen, major element composition  
81 (aluminum and silicon), and particle size distribution. Based on these novel samples and data sets, this study aims at  
82 1) determining the controls on POC content in the Huanghe; 2) tracing and quantifying the sources of riverine POC  
83 in the Huanghe; and 3) providing depth-integrated estimates of POC fluxes in the most turbid large river system.

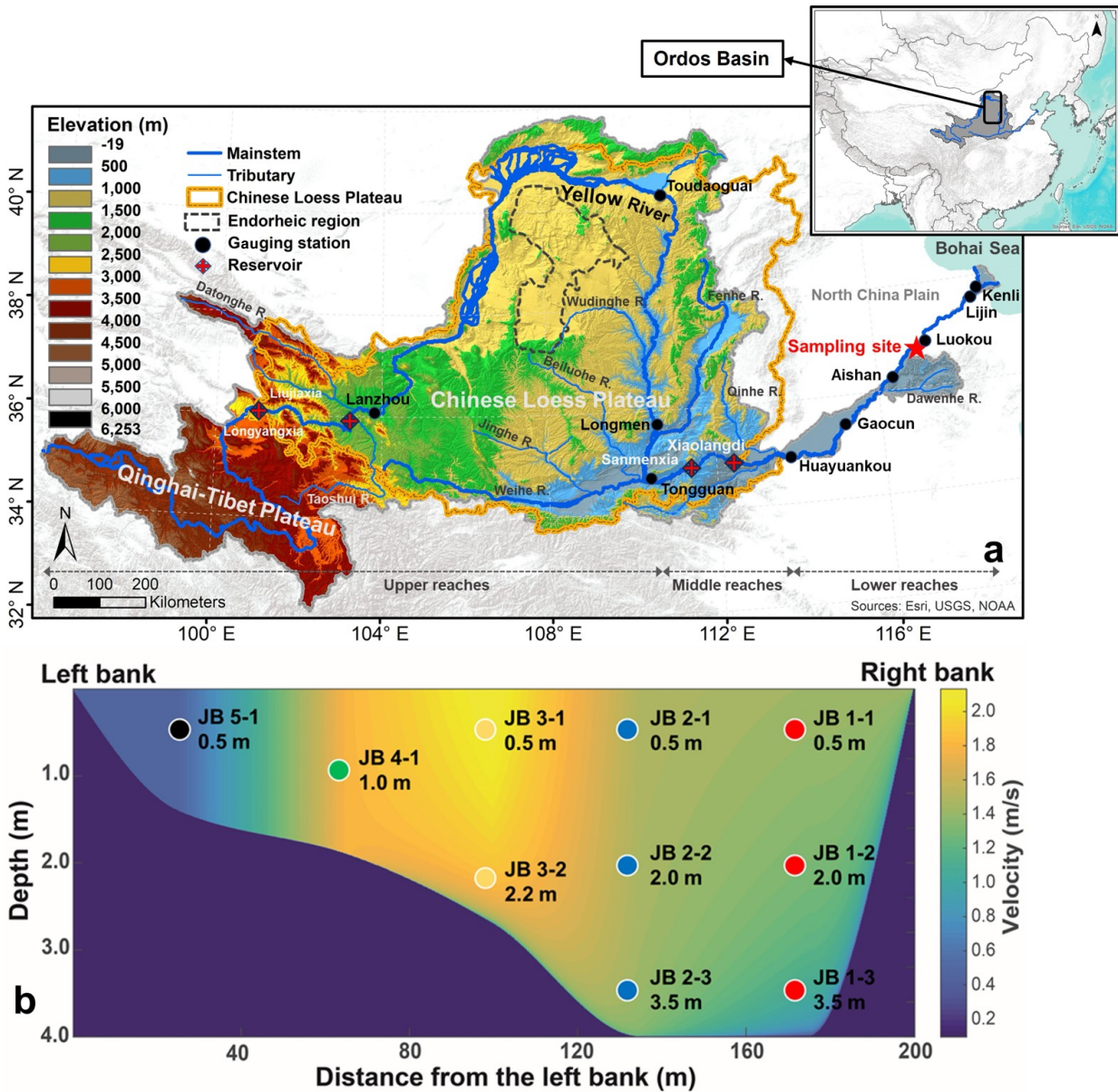
## 84 **2 Study area**

85 The Huanghe originates from the north-eastern Qinghai-Tibet Plateau (QTP) and runs through the Chinese Loess  
86 Plateau (CLP) and the North China Plain (NCP) to the Bohai Sea (Figure 1a). It is 5,464 km long and drains a basin  
87 area of  $79.5 \times 10^4$  km<sup>2</sup>. The Huanghe drainage basin can be subdivided into three main geomorphic units: 1) the high-  
88 relief upper reaches spanning from the source region (elevation of 4,500 m) to the city of Toudaoguai (located 3,472  
89 km downstream at an elevation of 1,000 m); 2) the middle reaches with a channel length of 1,206 km, ending at  
90 Huayuankou (elevation of 110 m) draining landscapes characterized by relatively gentle slopes; and 3) the lower  
91 reaches where the river flows eastwards across a fluvial plain over a length of 786 km. These three sections drain  
92 53.8%, 43.3%, and 2.9% of the whole Huanghe basin area, respectively (Wang et al., 2007; YRCC, 2016). Most  
93 second-order tributaries drain the CLP region and feed the main channel in the middle reaches, the Dawenhe River  
94 being the only tributary of the lower reaches, with negligible water and sediment supply due to upstream trapping in  
95 lakes and reservoirs. It is worth noting that more than 50% of the water discharge at the Huanghe's mouth comes from  
96 the QTP, whereas over 90% of the sediment load originates from the CLP (Wang et al., 2010, 2017; Pan et al., 2016).  
97 The CLP is thus the principal source area of sediment to the Huanghe (Shi and Shao, 2000; Guo et al., 2002; Wang  
98 and Fu et al., 2016).

99 The Huanghe drainage basin is mostly underlain by the North China craton, and is bounded by several mountain belts.  
100 The watershed encompasses 46% of sedimentary rock outcrops (mainly siliciclastic rocks with minor carbonates), and

101 about 45% of unconsolidated sediments (mainly Quaternary loess deposits). The remaining outcrops include  
102 metamorphic, plutonic, and volcanic rocks formed from the Archean to the Tertiary (Figure S1). Although river  
103 incision is strong in the QTP, a substantial part of the corresponding eroded material is not effectively transferred to  
104 the lower reaches due to deposition in the CLP and the western Mu-Us desert, a situation that has prevailed since at  
105 least the middle Pleistocene (Nie et al., 2015; Licht et al., 2016; Pan et al., 2016). In addition, recent anthropogenic  
106 disturbance such as constructions of large dams in the upper reaches has profoundly modified the export of solid  
107 materials from the basin (Wang et al., 2007). The Huanghe then flows through the CLP that has acted as the major  
108 supplier of sediment to the system since at least the Calabrian Pleistocene (Stevens et al., 2013; Bird et al., 2015).  
109 There, an easily erodible loess-paleosol formation has accumulated since 2.58 Ma (Guo et al., 2002), over a thickness  
110 ranging from a few meters to more than 500 m, with an average of 100 m. This loess-paleosol formation and underlying  
111 Cretaceous sedimentary rocks are actively incised by the main stem and its tributaries (Shi and Shao, 2000; Guo et  
112 al., 2002; Wang and Fu et al., 2016). Notably, the Ordos Basin underlying the CLP is rich in oil and gas (Guo et al.,  
113 2014). In the lower reaches, the river drains Quaternary fluvial deposits and sedimentary rocks.

114 The Huanghe drainage basin encompasses the entire arid and semi-arid region of northern China in the upper and  
115 middle reaches, and is characterized by more humid climate conditions in the lower reaches. Annual average  
116 precipitation (over the period 1950 - 2000) in the upper, middle and lower reaches regions is 368 mm, 530 mm, and  
117 670 mm, respectively (Wang et al., 2007). As a result of the East Asian summer and winter monsoon circulations, the  
118 rainy season (June to September) contributes 85% of the annual precipitation (Wang et al., 2007). During the rainy  
119 season, frequent storm events lead to concentrated flows (relatively high discharge) in vulnerable gully-hill systems,  
120 the dominant regional geomorphic landscape, and actively participates in soil erosion in the CLP (Shi and Shao, 2000;  
121 He et al., 2004; Qu et al., 2020). The present-day (2002 to 2016) suspended sediment flux delivered by the Huanghe  
122 to the sea is about 0.12 Gt/yr, which implies a decrease of nearly 90% in sediment export compared to the widely cited  
123 estimate of 1.08 Gt/yr (average value between 1950 to 1980, Milliman and Farnsworth, 2011). This massive decrease  
124 in sediment export mostly results from human perturbations, including soil conservation practices in the CLP and  
125 retention in large reservoirs, rather than from climatic variations such as the decreasing precipitation observed in the  
126 region over the last decades (Wang et al., 2007; Ran et al., 2013; Wang and Fu et al., 2016; Li et al., 2022). A scheme  
127 for water and sediment regulation (WSR) has been implemented through the construction of the Xiaolangdi Reservoir  
128 since 2002, aiming to mitigate water and sediment imbalances in the lower reaches. This regulation has resulted in a  
129 modification of the flux of sediment delivered to the lower reaches and estuary, making the Huanghe a highly human-  
130 regulated river system. However, no WSR was implemented in 2016, the year of our sampling campaign, suggesting  
131 that the collected SPM samples are not significantly affected by retention in dams, and thus are representative of the  
132 fluvial transport of terrestrial materials eroded from the CLP.



133  
 134 Figure 1: (a) Elevation map of the Huanghe drainage basin showing the main reservoirs and gauging stations along the  
 135 main stem as well as our sampling site (36.75°N, 117.02°E, near the Luokou gauging station); and (b) channel cross-section  
 136 sampled for this study showing the depth and lateral distribution of suspended particulate matter (SPM) samples and  
 137 modeled velocity distribution based on the "law of the wall", using the point velocity data measured by a current velocity  
 138 meter attached to the sampler.

### 139 3 Sampling and analytical methods

#### 140 3.1 Sampling strategy

141 Detailed sampling of a cross-section of the Huanghe was carried out on the 17<sup>th</sup> of July, 2016, during the flood season  
 142 (Figure S2). Samples were collected along five depth profiles near the Luokou hydrological station (36.75°N, 117.02°E),  
 143 250 km upstream from the river mouth (Figure 1). This sampling strategy allows for accessing the full range of  
 144 suspended sediment particle size (Bouchez et al., 2014). The cross-section is 200-meters wide at the surface and 4

145 meters deep at most (Figure 1; YRCC, 2016). As in previous studies, we used a home-made, 10-liter, point-sediment  
146 horizontal Niskin-type sampler attached to a current velocity meter, to collect river water samples and measure the  
147 water velocity simultaneously. Subsequently, two water samples were collected at the surface near the right bank in  
148 May and June 2017 before the flooding season, to retrieve fine suspended particulate matter. For each sample,  
149 approximately 30 liters of river water were collected and were then filtered through pre-weighed 0.22- $\mu\text{m}$  porosity  
150 cellulose acetate membrane filters within 24 hours. After rinsing the filters with filtered water, all sediment samples  
151 were transferred into centrifuge tubes and freeze-dried before weighing and analysis. A bed sediment (BS) sample  
152 was collected on an exposed, recently flooded sediment bar of the riverbed.

### 153 **3.2 Physical and geochemical analysis**

154 Apart from a 50-mg aliquot of SPM samples preserved for particle size analysis, samples were finely ground using an  
155 agate mortar and pestle prior to chemical and isotopic analyses. The particle size distribution of the unground aliquots  
156 was measured using a Laser Diffraction Particle Size Analyzer (Beckman Coulter LS-12 320) at the École Normale  
157 Supérieure (ENS), Paris, France. Before analysis, unground SPM aliquots were dispersed in deionized water and then  
158 in sodium hexametaphosphate in an ultrasonic bath. For each sample, we measured three replicates and report the  
159 average median particle size (D50,  $\mu\text{m}$ ) with an uncertainty better than 2% (Table 1). The chemical composition of  
160 SPM samples was measured on ground aliquots at the Centre de Recherches Pétrographiques et Géochimiques  
161 (CRPG), Vandoeuvre-lès-Nancy, France, using inductively coupled plasma atomic emission spectroscopy (ICP-OES)  
162 for major elements with typical uncertainties of 3% (Carignan et al., 2001).  
163 For particulate organic carbon content (POC%, wt.), stable carbon isotope  $\delta^{13}\text{C}$  (in ‰<sub>VPDB</sub>, *i.e.*, in ‰ relative to Vienna  
164 Pee Dee Belemnite) and radiocarbon isotope  $\Delta^{14}\text{C}$  (expressed as fraction modern, Fm), ground homogenized samples  
165 were fumigated using 12M HCl fumes in a closed Teflon tank at 60 °C for 48 hours to remove the carbonate fraction,  
166 and were then dried under vacuum prior to analysis. Total nitrogen content (TN%, wt.) was measured on non-acidified  
167 samples (Komada et al., 2008). Triplicate analysis on POC% and  $\delta^{13}\text{C}$  of POC (acidified aliquots) as well as TN%  
168 (non-acidified aliquots) were carried out on an Organic Elemental Analyzer (OEA) coupled with Isotope Ratio Mass  
169 Spectrometry (IRMS, Thermo Scientific Flash 2000) under continuous flow mode at Géosciences Paris Saclay  
170 (GEOPS), Orsay, France. Subjected to the blank subtraction by linearity test, two international standards including  
171 USGS-40 and IAEA-600 as well as an internal standard (GG-IPG) were used to build linear regression equations to  
172 calibrate the elemental and isotopic values for both carbon and nitrogen. Uncertainties on POC%,  $\delta^{13}\text{C}$ , and TN%,  
173 based on replicate measurements ( $1\sigma$ ,  $n=3$ ), are lower than 0.02%, 0.06‰, and 0.02‰, respectively. The  $^{14}\text{C}$  activity  
174 of POC was measured on a new compact accelerator mass spectrometry (AMS), *ECHoMICADAS* (Hatté et al., 2023),  
175 using a gas ion source interface system (GIS) at the Laboratoire des Sciences du Climat et de l'Environnement (LSCE),  
176 Gif-sur-Yvette, France, with an absolute uncertainty of max  $\pm 0.5\%$ . Aside from the gas bottles of prepared blank PhA  
177 and standard NIST OX II which are permanently connected to the GIS and, used for normalization and corrections for  
178 fractionation and background, international standards including IAEA-C5, IAEA-C7, IAEA-C8, and blank PhA were  
179 prepared in different sizes (10 to 100's  $\mu\text{g C}$ ) to match the amount of OC found in the sediment samples.

### 180 3.3 POC source apportionment

181 To quantify the contribution and associated uncertainties of various sources to POC transported in the Huanghe, a  
182 Bayesian Markov Chain Monte Carlo (MCMC) based on a three-end member (Appendix A) mixing scheme was  
183 adopted. This approach considers the variability on each end member contribution, assuming this variability can be  
184 represented by a normal distribution. We computed the *a posteriori* distribution of the Bayesian formulation using the  
185 MCMC method, using the MixSIAR package (Moore & Semmens, 2008; Stock & Semmens, 2016). All computations  
186 were performed in the R environment (<http://www.r-project.org/>). To ensure reliable simulation, the model was run  
187 with chain length of 300,000 by 3 chains, using a burn-in of 200,000 steps, and a data thinning of 100 for each sample.  
188 The mixing model was constructed on the dual stable and radioactive isotope of the riverine POC pool ( $\delta^{13}\text{C}$  and  $\Delta^{14}\text{C}$ )  
189 and of the three potential source pools (Section 5.2) by the following equations:

$$\begin{aligned} \text{Isotope\_ratio}_{\text{sample}} &= \sum_{\text{source}} (f_{\text{source}} * \text{Isotope\_ratio}_{\text{source}}) \\ \sum_{\text{source}} f_{\text{source}} &= 1 \end{aligned}$$

192 where  $\text{Isotope\_ratio}_{\text{sample}}$  is either the  $\delta^{13}\text{C}$  or  $\Delta^{14}\text{C}$  value of the sample,  $\text{Isotope\_ratio}_{\text{source}}$  is either the  $\delta^{13}\text{C}$  or  
193  $\Delta^{14}\text{C}$  value of different possible sources of POC and  $f_{\text{source}}$  is the relative contribution of each source of POC. Further  
194 model diagnostics was performed using Gelman-Rubin and Geweke test, both diagnostics validated the robustness  
195 and convergency of the model.

### 196 3.4 Depth-integrated fluxes

197 Instantaneous depth-integrated fluxes of SPM and POC sources were calculated for the cross-section using a method  
198 developed by Bouchez et al. (2011a, b). This method is based on the systematic variation of SPM concentration in the  
199 water column (Figure 2) applying a Rouse-based model (Rouse, 1937). We first constructed a bathymetric profile of  
200 the river cross-section based on the depth information collected in the field and then modeled the velocity distribution  
201 across the transect (Figure 1b) through fits of the so-called "law of the wall" to water velocity measured at the location  
202 of each sample within the cross-section using a current meter. Afterward, the concentration of total SPM and various  
203 particle size fractions could be estimated by applying the so-called Rouse model (Rouse, 1937) to each particle size  
204 fraction separately (Bouchez et al., 2011a), resulting in a map of the particle size distribution in the river cross-section  
205 (Figure S3). The aluminum to silicon ratio (Al/Si mass ratio) is inversely related to the particle size of river SPM in  
206 the Ganges-Brahmaputra, the Amazon, and the Mackenzie Rivers (Galy et al., 2007; Bouchez et al., 2014; Hilton et  
207 al., 2015). Such a linear relationship between D50 and Al/Si was also observed in our dataset, allowing for computing  
208 the spatial distribution of POC content in the cross-section, based on the linear relationship between POC and Al/Si  
209 (Figure 3). Finally, combining modeled water velocity, SPM concentration, and POC distribution we calculated a  
210 depth-integrated, instantaneous POC flux for the whole river channel (Figure S3, detail in supplementary material).

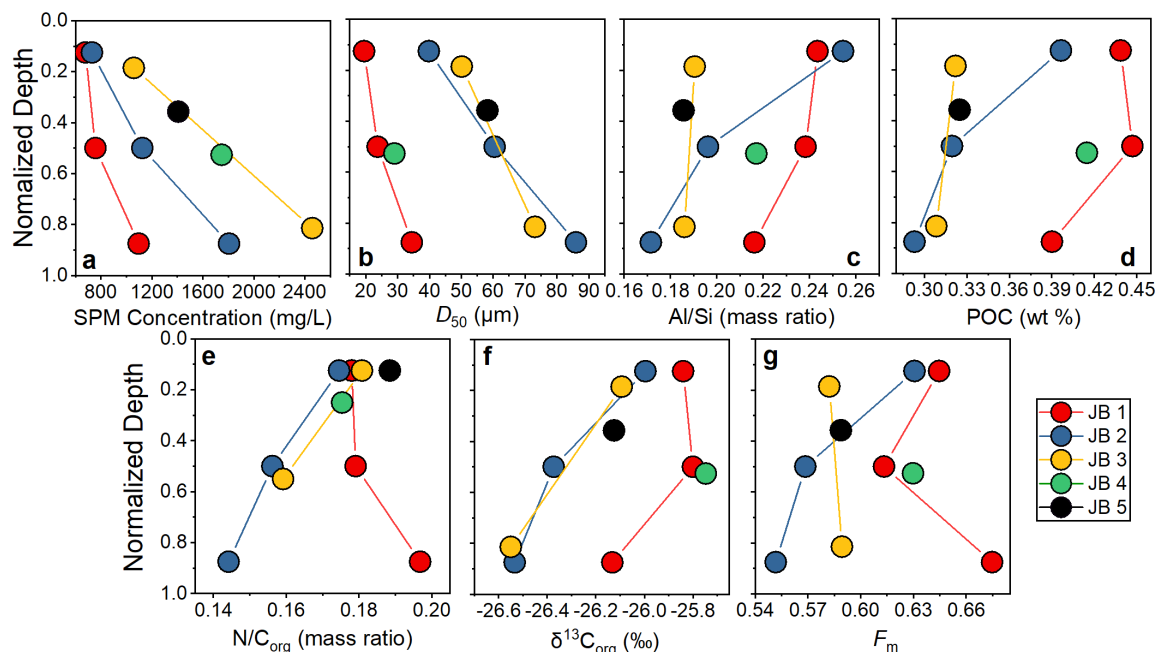
## 211 4 Results

212 We report the first isotopic dataset of POC samples collected along several depth profiles distributed over a cross-  
213 section of the Huanghe (Table 1, n=10). SPM concentrations range from 679 to 2,459 mg/L (avg.  $1,286 \pm 572$  mg/L,  
214 reported with mean value with one standard deviation, herein after) and show an obvious increase from the surface to  
215 the bottom and from the right bank to the left bank (Figure 1b and 2a). The surface SPM concentration (*i.e.*, samples  
216 collected 0.5 m below the surface) decreases laterally as the water column deepens. The range of measured Huanghe  
217 SPM D50, *i.e.* the median particle size (19.5-86.0  $\mu\text{m}$ , Figure 2b) agrees with that of SPM collected at Lijin (16.6-  
218 120.1  $\mu\text{m}$ , n=50) during the same flooding season by Moodie et al. (2022). In each depth profile, SPM is consistently  
219 coarsening with depth as revealed by the evolution of grain size parameters such as D10, D50, and D90 (Table 1,  
220 Table S1, Figure 2 and Figure S4). The finest SPM is transported on the right bank and at the surface, while the  
221 coarsest SPM is found at the bottom of the middle profile (sample JB 2-3). Two types of depth profiles can be  
222 distinguished at Luokou based on particle size distributions (Figure S4) and the relationship between D50 and water  
223 depth (Figure 2b). On the one hand, the JB 1 and JB 4 profiles show a well-marked, bi-modal distribution of particle  
224 size (Figure S4) together with relatively low and consistent D50 (Figure 2b). On the other hand, the JB 2, JB 3, and  
225 JB 5 profiles show a more unimodal distribution of particle size (Figure S4) and a unique D50 - sampling depth  
226 relationship (Figure 2b). Interestingly, these two groups can also be distinguished in terms of relationships between  
227 POC% and  $\delta^{13}\text{C}$  with water depth (Figures 2d, 2f). As expected, the Al/Si ratio is well-related to the particle size, and  
228 the ratios measured in the middle profile SPM samples (0.17 for JB 2-3 and 0.26 for JB 2-1) encompass the full range  
229 of Al/Si found in the whole cross-section (Figure 2c). The relatively low Al/Si ratios are comparable to that of the  
230 middle Huanghe (Qu et al., 2020) and other large turbid river systems such as the Ganges-Brahmaputra (Galy et al.,  
231 2008b), Salween, and Irrawaddy (Tipper et al., 2021).

232 SPM in the Huanghe is characterized by low TN and POC content (wt.%), ranging from 0.04% to 0.08% ( $0.06 \pm$   
233  $0.01\%$ ) and from 0.29% to 0.42% ( $0.37 \pm 0.06\%$ ), respectively (Figure 2d; Table 1). POC content generally decreases  
234 from the surface to the river bed, with quantitative differences from one profile to another (Figure 2d). Notably, the  
235 JB 1 profile shows the highest POC% and TN%. In addition, the ratio of TN% to POC%:  $\text{N}/\text{C}_{\text{org}}$  increases with depth  
236 in the JB 1 profile (from top to bottom), while it decreases in the JB 2 and JB 3 profiles (Figure 2e). The  $\delta^{13}\text{C}$  of POC  
237 varies over a narrow range from  $-26.55\%$  to  $-25.75\%$  ( $-26.12 \pm 0.29\%$ , Figure 2f) and becomes lighter with depth,  
238 showing that fine SPM has higher  $\delta^{13}\text{C}$  than coarse SPM. These values are lower than those previously reported for  
239 other Huanghe sampling sites upstream:  $-24.7 \pm 0.4\%$  at Toudaoguai,  $-24.9 \pm 0.6\%$  at Longmen, and  $-23.8 \pm 0.6\%$   
240 at Lijin (Qu et al., 2020, Hu et al., 2015; Tao et al., 2015; Yu et al., 2019a; Ge et al., 2020). The radiocarbon activity  
241 of POC of the Huanghe at Luokou is relatively low (Figure 2g), with  $F_m$  ranging from 0.552 ( $\Delta^{14}\text{C} = -453\%$ ; sample  
242 JB2-3) to 0.675 ( $\Delta^{14}\text{C} = -331\%$ ; sample JB1-3), spanning from 3,160 to 4,780  $^{14}\text{C}$  yrs, and the average value is  $0.607$   
243  $\pm 0.038$  ( $\Delta^{14}\text{C} = -412 \pm 37.6\%$ , n=10). This range of radiocarbon activity is consistent with published values for POC  
244 collected at the river surface downstream of Toudaoguai (Qu et al., 2020). All the POC radiocarbon activity data  
245 reported so far for the Huanghe are comparable to mean values for Arctic large rivers ( $\Delta^{14}\text{C} = -397\%$ , ca. 4,480  $^{14}\text{C}$   
246 yrs, Ke et al., 2022), revealing the multimillennial-age nature of POC transported by the Huanghe. The elemental and  
247 isotopic signatures of the two fine SPM samples HH 17.05 and HH 17.06 (on average POC% = 1.07%,  $\delta^{13}\text{C} =$



248  $-25.67\%$ ,  $F_m = 0.720$ ; and  $Al/Si = 0.37$ ) are significantly different from those of the depth profile samples (Table 1).  
 249 The bed sediment sample has a comparatively low POC% (0.21%),  $\delta^{13}C$  ( $-27.35\%$ ),  $F_m$  (0.099), and  $Al/Si$  ratio  
 250 (0.17).



251  
 252 **Figure 2: Variation of physical and chemical parameters in the river cross-section, shown as a function of sampling depth**  
 253 **normalized to total depth of the water column at the location of the considered depth-profile, for the Luokou cross-section**  
 254 **on the Huanghe (June 16, 2017). (a) SPM concentration; (b) particle size distribution (shown as D50); (c) Al/Si mass ratio;**  
 255 **(d) POC content (weight %); (e) N/C<sub>org</sub> mass ratio; (f) stable carbon isotope ratio  $\delta^{13}C_{org}$  (‰); (g) radiocarbon activity  $F_m$ .**

256 **Table 1: SPM characteristics and POC properties of the river-cross-section sampling.**

Sample ID	Type	Depth (m)	SPM mg/L	POC (%)	SD	$\delta^{13}C_{org}$ (‰)	SD	$F_m$	$\Delta^{14}C$ (‰)	SD	$^{14}C$ age	TN (%)	N/C <sub>org</sub>	Al/Si	D50 $\mu m$
JB 1-1	SPM	0.5	679	0.44	0.02	-25.84	0.03	0.645	-360	7	3527	0.078	0.178	0.243	19.5
JB 1-2	SPM	2	757	0.45	0.01	-25.80	0.06	0.613	-392	11	3929	0.080	0.179	0.238	23.7
JB 1-3	SPM	3.5	1095	0.39	0.01	-26.13	0.04	0.675	-331	7	3161	0.077	0.197	0.216	34.5
JB 2-1	SPM	0.5	730	0.40	0.03	-26.00	0.01	0.631	-374	7	3703	0.069	0.175	0.255	39.8
JB 2-2	SPM	2	1124	0.32	0.01	-26.37	0.06	0.569	-436	13	4537	0.050	0.156	0.196	60.4
JB 2-3	SPM	3.5	1806	0.29	0.01	-26.53	0.06	0.552	-453	38	4779	0.042	0.144	0.172	86.0
JB 3-1	SPM	0.5	1058	0.32	0.02	-26.09	0.03	0.582	-422	12	4346	0.058	0.181	0.190	50.1
JB 3-2	SPM	2.2	2459	0.31	0.02	-26.55	0.04	0.589	-415	11	4247	0.049	0.159	0.186	73.1
JB 4-1	SPM	1	1747	0.41	0.02	-25.75	0.06	0.630	-375	8	3714	0.073	0.175	0.217	29.0
JB 5-1	SPM	0.5	1406	0.32	0.01	-26.12	0.05	0.589	-416	11	4256	0.061	0.188	0.186	58.2
HH 17.05	SPM	0	83	0.92	0.00	-25.73	0.14	0.711	-295	19	2740	0.184	0.200	0.358	5.2
HH 17.06	SPM	0	54	1.21	0.01	-25.60	0.07	0.729	-277	25	2539	0.261	0.215	0.377	4.3
HH	BS			0.21	0.03	-27.35	0.05	0.099	-901	7	18539	0.019	0.087	0.175	44.4

## 257 5 Discussion

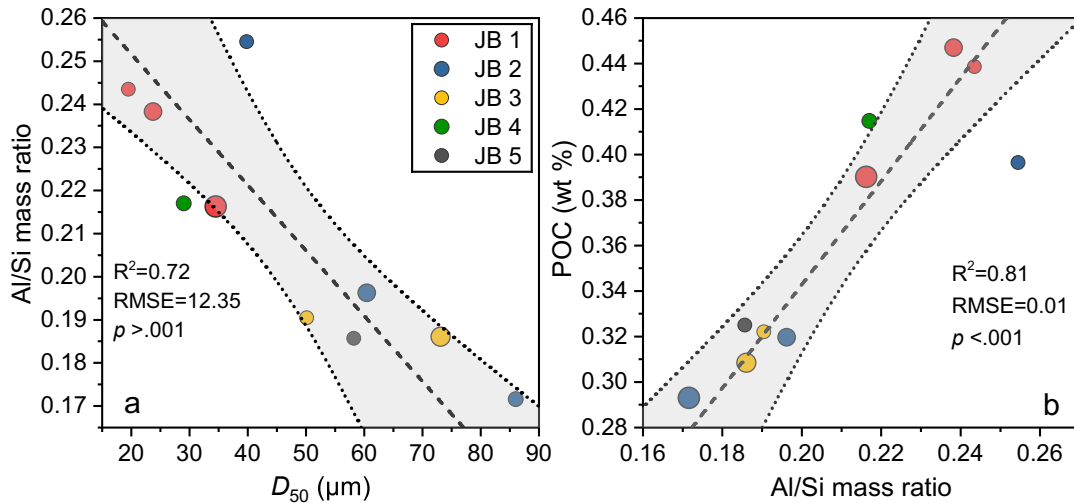
258 We observe significant heterogeneities of elemental and isotopic carbon composition as well as inorganic chemistry  
 259 over the studied river cross-section. The possible mechanisms behind these variations are assessed hereafter. Then,  
 260 sources of riverine POC are determined and quantified, confirming that erosion of the loess-paleosol sequence of the

261 CLP is a major source of aged and refractory biospheric OC to the Huanghe. Finally, we assess the POC load and its  
 262 variability over the transect profile, inferring the importance of the supply of POC from the river bottom in the  
 263 Huanghe.

## 264 5.1 Transportation mode of POC in the Huanghe

### 265 5.1.1 POC loading and its controls

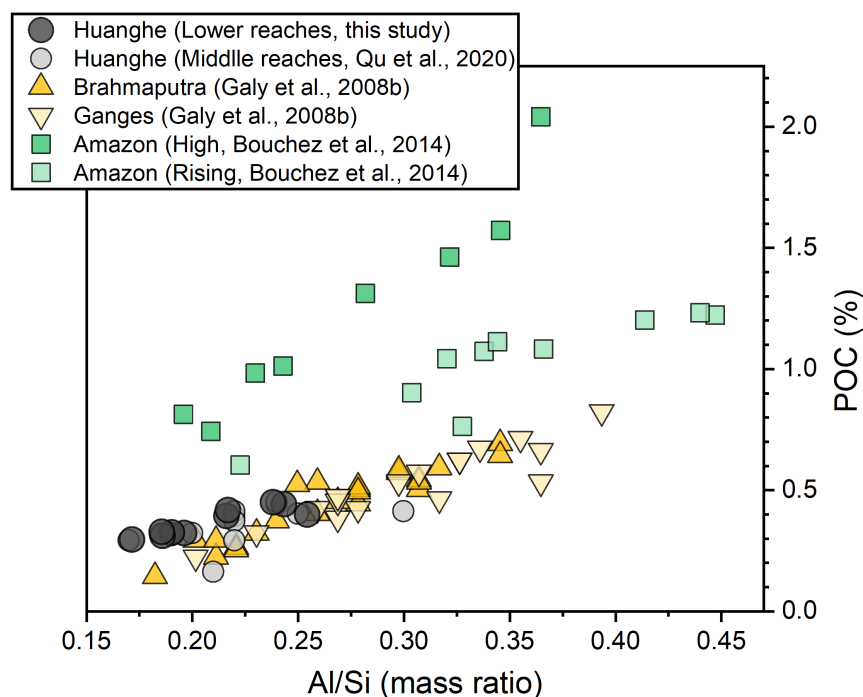
266 The Huanghe is characterized by a high SPM load with relatively low POC% ( $0.37 \pm 0.06\%$ ,  $n=10$ ). In the Luokou  
 267 cross-section, POC content generally increases with decreasing particle size (Figure S5), with the two clay-sized  
 268 ("HH") samples showing the largest POC content (Table 1). Consistently, the Al/Si ratio of Huanghe sediments, which  
 269 varies as an inverse linear function of the median particle sizes  $D_{50}$  ( $R^2=0.72$ ,  $p > .001$ , Figure 3a), positively correlates  
 270 with POC% ( $R^2=0.81$ ,  $p < .001$  Figure 3b), a pattern observed globally (Galy et al., 2008b; Bouchez et al., 2014; Hilton  
 271 et al., 2015; Repasch et al., 2021). This pattern is consistent with POC variability in the Huanghe reported for manually  
 272 separated size fractions of sediments (Yu et al., 2019b).



273  
 274 **Figure 3: Relationships between (a) particle size  $D_{50}$  and Al/Si mass ratio; (b) Al/Si mass ratio and POC content for the**  
 275 **Luokou cross-section on the Huanghe (July 17, 2016). The symbol size indicates the sampling depth in the water column,**  
 276 **with symbol size increasing with depth. The shaded area represents the 95% confidence area of the linear best-fit (black**  
 277 **dashed line), the upper and lower bound are marked by grey dotted lines.**

278 The first reason for the low POC content of Huanghe sediments is therefore their relatively low values of Al/Si  
 279 compared to other systems - a feature than can be related to the quartz-rich, OC-poor nature of the loess-paleosol  
 280 formations of the CLP (Jahn et al., 2021; Huang and Ren, 2006; He et al., 2006; Ning et al., 2006; Wang and Fu,  
 281 2016). However, Huanghe sediments are relatively poor in POC, even considering their low Al/Si, compared to other  
 282 rivers globally. To that effect, the so-called "POC loading" can be characterized by the slope described by sediment  
 283 data in an Al/Si-POC diagram (Galy et al., 2008b; Figure 4). For a given Al/Si ratio, the POC% in the Luokou cross-  
 284 section is similar to that of the middle Huanghe (Qu et al., 2020), indicating the relatively invariant transport mode of  
 285 POC between the middle and lower reaches. Previous studies have shown that the positive relationship between POC%  
 286 and Al/Si can be partially explained by OC adsorption onto the mineral surface (Curry et al., 2007; Galy et al., 2008b;  
 287 Blair and Aller, 2012; Bouchez et al., 2014; Qu et al., 2020). In the loess-paleosol deposits acting as a source of

288 sediments to the Huanghe, OC is mostly preserved and stabilized by forming organo-aggregates with kaolinite and  
 289 through adsorption onto iron oxides (Wang et al., 2013).  
 290 However, POC loading in the Huanghe is small compared to that of the Amazon (Bouchez et al., 2014), but similar  
 291 to that of the Ganges-Brahmaputra system (Galy et al., 2008b). While many factors could influence POC loading  
 292 across these catchments, we note that another similarity between the Huanghe and Ganges-Brahmaputra fluvial  
 293 systems is their millennial-aged OC<sub>bio</sub> (Galy et al., 2007; Tao et al., 2016). This is in stark contrast with the Amazon,  
 294 where younger OC<sub>bio</sub> ages have been reported (Bouchez et al., 2014). Given that younger OC<sub>bio</sub> recently  
 295 photosynthesized in terrestrial or aquatic ecosystems can be readily oxidized within catchments (Mayorga et al., 2005),  
 296 the relatively low POC loading observed at the mouth of the Ganges-Brahmaputra and the Huanghe (Figure 4) could  
 297 be related to the predominance of refractory, aged OC<sub>bio</sub> and OC<sub>petro</sub> in those systems, while the Amazon sediments  
 298 would still contain significant amount of younger, more labile OC<sub>bio</sub>.



299  
 300 **Figure 4: "POC loading" of river SPM of large rivers. The POC loading is estimated from the slope of the relationship**  
 301 **between POC content and the Al/Si ratio of each fluvial system (Galy et al., 2008b). All SPM samples were collected along**  
 302 **depth profiles except for the middle Huanghe (Qu et al., 2020).**

303 In detail, and as explained in more detail below (**Section 5.1.2**) we also observe a significantly different POC loading  
 304 between the JB 1 and JB 2 depth profiles at the Luokou station (Figure 3). This difference in POC loading in the cross-  
 305 section of the Huanghe might indicate the delivery of recent OC<sub>bio</sub>, specifically near the right bank (the closest to the  
 306 JB 1 profile) for the Luokou site, a scenario which is supported by the comparatively younger age of POC in profile  
 307 JB 1. Consistently with this interpretation, temporally variable POC loading at a given site has been reported for the  
 308 Amazon (Bouchez et al., 2014), where higher POC loading during the high-water stage compared to the rising water  
 309 stage has been attributed to the erosion of discrete organic debris from riverbanks.

310 Variable POC loading amongst large catchments has implications for evaluating the likelihood of POC preservation  
 311 in estuaries. The Ganges-Brahmaputra system delivers relatively old, refractory OC<sub>bio</sub> to the Bengal Fan with an almost

312 complete burial efficiency (Galy et al., 2007). Given the observed similarity in POC loading and age, we can thus  
313 expect a similar, efficient preservation for the Huanghe offshore depositional system. In addition to the low reactivity  
314 of the POC transported by the Huanghe, the high sediment accumulation rates in the Huanghe coastal domain might  
315 further inhibit OC oxidation (Blair and Aller, 2012). Consequently, the case of the Huanghe differs drastically from  
316 that of the Amazon, where higher POC loading is observed, with a larger contribution of young, labile OC<sub>bio</sub> either as  
317 discrete organic matter or associated with mineral surfaces, leading to low POC burial efficiency in the ocean  
318 (Bouchez et al., 2014; Blair and Aller, 2012).

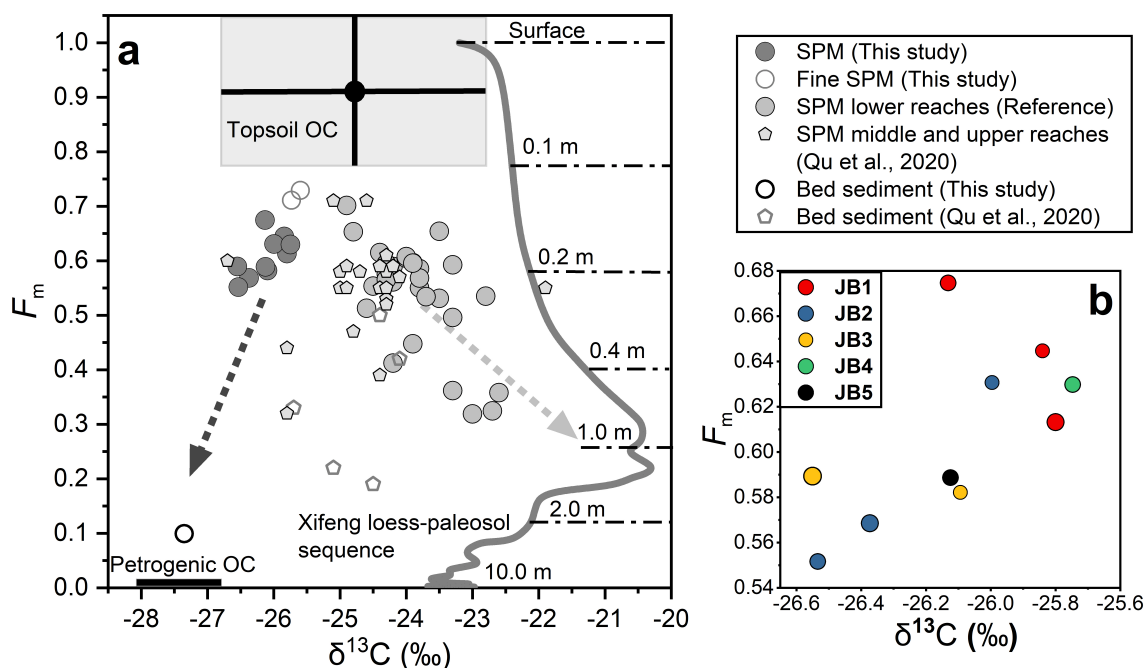
### 319 **5.1.2 Chemical heterogeneity within the transect**

320 There is clear lateral and vertical variability of POC content and SPM inorganic chemistry across the Luokou cross-  
321 section of the Huanghe. For each vertical depth profile, clay-rich fine particles are transported near the channel surface,  
322 and quartz-rich coarse particles flow near the river bottom. Accordingly, the Al/Si ratio, POC content and POC  
323 radiocarbon activity generally decrease with depth. Elemental (POC%) and isotopic POC signatures (<sup>13</sup>C and <sup>14</sup>C) are  
324 inversely related to the particle size (D<sub>50</sub>; Figure S5). These patterns are observed in other large fluvial systems, e.g.,  
325 Ganges and Brahmaputra, Amazon and Mackenzie (Galy et al., 2008b; Bouchez et al., 2014, Hilton et al., 2015),  
326 showing that hydrodynamic sorting is the primary control on suspended sediment OC content, segregating inorganic  
327 and organic material according to particle size (Bouchez et al., 2011a, 2014).

328 At the Luokou sampling site, lateral variability at the channel surface shows that POC-rich fine particles are  
329 preferentially transported near the right bank (Figure 2 and Figure S3). This pattern is validated by the Rouse model  
330 provided in Text S1, the Rouse number ( $Z_R$ ) is 0.137, 0.236, and 0.284 for JB-1, JB-2, and JB-3, respectively. In  
331 essence,  $Z_R$  can reflect the balance between gravitation settling and upward turbulent diffusion.  $Z_R$  is smaller near the  
332 right bank while larger near the left bank, showing heterogeneity across the transect. Larger particles exhibit a faster  
333 settling velocity due to their increased weight, leading to a higher  $Z_R$ . On the other hand, the lighter ones settle more  
334 slowly, resulting in  $Z_R$  approaching 0. This means that their concentration remains relatively constant along a given  
335 depth profile. However, as depth increases and the concentration of larger particles grows, the proportion of these  
336 finer particles in the overall sediment decreases (Bouchez et al., 2011a). The channel geometry thus needs to be  
337 examined as a potential factor to produce such lateral heterogeneity, in particular the mechanisms of bed sediment  
338 resuspension and bank erosion.

339 Resuspension of bed sediments is also a possible mechanism that could explain the lateral heterogeneity in POC  
340 content in the study cross-section of the Huanghe. Indeed, scouring of channel bed sediment at high water flow may  
341 also shift POC to more negative radiocarbon and stable isotope signatures. Our sample set collected in July 2016  
342 during a flooding period (water flow velocity up to 2.1 m/s, Figure 1) supports this scenario. Indeed, the increase in  
343 D<sub>50</sub> of surface SPM samples from right to the left bank, that is with total channel depth decrease, is consistent with  
344 coarse sediment resuspension from the bed. This is also supported by the Rouse model, where higher  $Z_R$  in the shallow  
345 water near the left bank indicates a greater likelihood of sediment settling to the bed, lower  $Z_R$  suggests that there is  
346 enhanced SPM supply from the riverbed. Such a scenario is also supported by the three-fold increase in SPM flux

347 observed from the upstream Huayuankou station to the downstream Lijin station in July 2016, despite a four-fold  
 348 decrease in water discharge (Figure S2).  
 349 Bank erosion can be a significant mechanism for the delivery of sediments to river systems (Guo et al., 2007). Bank  
 350 erosion at Luokou would make OC from the lower Huanghe alluvial plain a potential source of POC in the lower  
 351 reaches of the Huanghe. Frequent inundation to the adjacent riparian zones in flooding seasons, surface runoff driven  
 352 by storm events, and agriculture irrigation etc., can mobilize young soil OC and discrete organic matter debris (*e.g.*,  
 353 plant-driven debris) to riverine POC (Hilton et al., 2011; Turowski et al., 2016). This mechanism provides a possible  
 354 explanation for the opposite trends displayed by samples from the JB 1 and JB 2 profiles in the  $F_m$  vs.  $\delta^{13}C$  space  
 355 (Figure 5). The youngest POC was found at the bottom of the JB 1 profile (JB 1-3). Meanwhile, the JB 1 samples have  
 356 comparatively higher  $N/C_{org}$  ratios and  $N\%$ , consistent with the input of discrete plant-derived debris from the bank  
 357 in addition to rock-derived detrital clastic material in the coarse fractions ( $> 32 \mu m$ , Yu et al., 2019b). The transport  
 358 and entrainment of plant debris deep in the water column has been evidenced in many large river systems, such as the  
 359 Amazon (Feng et al., 2016), the Ganges-Brahmaputra (Lee et al., 2019), the Mackenzie (Schwab et al., 2022), the Rio  
 360 Bermejo River (Repasch et al., 2021). Such input would also provide an explanation for the higher POC loading of  
 361 the JB 1 profile (Section 5.1.1).



362  
 363 **Figure 5:** (a)  $^{14}C$  activity (expressed as  $F_m$ ) vs.  $\delta^{13}C$  for a compilation of POC data collected over the 2011-2016 period in  
 364 the lower Huanghe, including samples from this study and previous studies at Huayuankou, Lijin, and Kenli (Hu et al.,  
 365 2015; Tao et al., 2015; Yu et al., 2019a; and Ge et al., 2020); SPM and bed sediment (BS) collected by Qu et al., 2020 at  
 366 Toudaoguai (most downstream location of the upper reaches) and Longmen in the middle reaches (Table S1). The grey  
 367 curve corresponds to  $\delta^{13}C_{org}$  of the top 10 m of the Xifeng loess-paleosol (Ning et al., 2006), and the corresponding  $F_m$  was  
 368 calculated from  $^{10}Be$ -derived ages following 'Age =  $-8033 * \ln(F_m)$ '. The soil depth is marked above the dot-dash line (Zhou  
 369 et al., 2010). Topsoil OC represents OC from the upper 10 cm of the loess-paleosol sequence with standard deviation marked

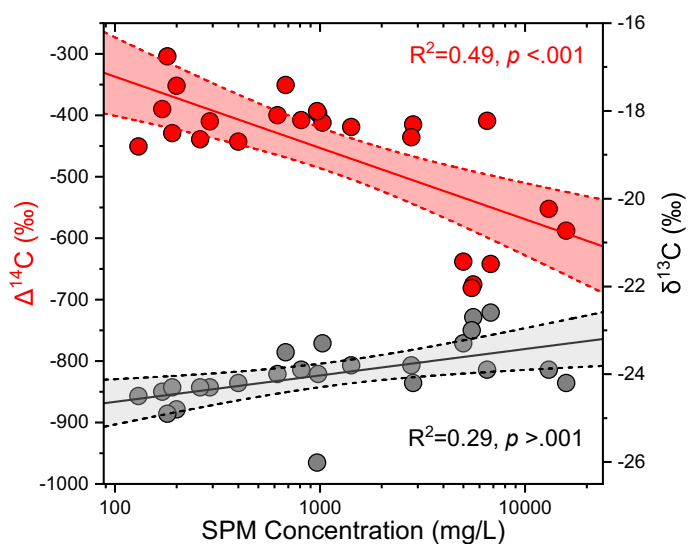
370 with black lines. (b)  $^{14}\text{C}$  activity (expressed as Fm) vs.  $\delta^{13}\text{C}$  diagram for the Huanghe sediment samples collected in this  
371 study at the Luokou cross-section. Symbol size increases with sampling depth in the water column.

## 372 5.2 POC provenance in the Huanghe: the significance of loess-paleosol-derived OC

### 373 5.2.1 Physical erosion of the loess-paleosol sequence

374 Over decennial to centennial time scales, the POC export of the Huanghe is mainly controlled by erosion of the CLP.  
375 Throughout the Quaternary, the erosion rate in the Huanghe basin has been mainly driven by climate shifts until human  
376 activities started and profoundly impacted sediment fluxes in the mid-Holocene (He et al., 2006). The Huanghe has  
377 experienced a 90% decrease in annual sediment load since the 1950s (Wang et al., 2015), caused by weakened soil  
378 erosion to the CLP and sediment retention by dams (Wang et al., 2007; Ran et al., 2013; Wang and Fu et al., 2016; Li  
379 et al., 2022). To determine the contributions of the various terrestrial OC components to Huanghe POC, we compiled  
380 published POC carbon isotope data for sediments collected in the lower reaches from 2011 to 2016, after the  
381 Xiaolangdi Reservoir was operated (Figures 5 and 6). This dataset shows that the radiocarbon ages of Huanghe POC  
382 are considerably old ( $5,100 \pm 1,700$   $^{14}\text{C}$  yrs,  $n=29$ ), with a minor fraction of modern photosynthesized  $\text{OC}_{\text{bio}}$  (Tao et  
383 al., 2015; Yu et al., 2019a, b). This relatively  $^{14}\text{C}$ -depleted POC suggests the significant contribution of OC originated  
384 from deep soil horizons within the catchment. Given that loess is easily erodible and that there is widespread gully  
385 erosion in the catchment, more intensive erosion of the CLP can mobilize more soils as well as older OC from deep  
386 soil horizons to fluvial transport. Therefore, higher sediment load in the river can be characterized by radiocarbon-  
387 depleted POC. This is evidenced by the negative trend between  $^{13}\text{C}$  and Fm of POC for sediment samples collected in  
388 the Huanghe over the 2011-2016 period (Figure 5a), suggesting that deep horizons of the loess-paleosol formations  
389 are a plausible source for the  $^{14}\text{C}$ -depleted end member. Besides, the preferential erosion of bomb carbon affected,  
390 recently photosynthesized and possibly degraded  $\text{OC}_{\text{bio}}$  from the overlying topsoils ( $< 10$  cm) most likely contributes  
391 to riverine POC (Tao et al., 2015).

392 As such, variable contribution of aged and radiocarbon-free OC from deep horizons of loess-paleosol formations of  
393 the CLP should have a significant impact on the elemental and isotopic signature of POC in the lower Huanghe.  
394 Erosion of loess-paleosol can also explain the decreasing POC% with increasing SPM concentration at different sites  
395 of the main channel (Ran et al., 2013; Qu et al., 2020), the negative relationship between SPM concentration and  
396 corresponding POC Fm at Luokou ( $R^2=0.49$ ,  $p < .001$ , Figure 6), and the low POC loading of the Huanghe (Section  
397 5.1.1), as the deep horizons of the loess-paleosol sequences are OC-poor, and mostly host OC that is highly degraded  
398 and refractory (Liu et al., 2012; Wang et al., 2013; Cheng et al., 2020). However, the slight increase of POC  $\delta^{13}\text{C}$  with  
399 increasing SPM concentration ( $R^2=0.29$ ,  $p > .001$ ) might indicate a significant supply of soil OC from loess-paleosol  
400 shallower depth, as inferred from the  $\delta^{13}\text{C}$  variation within the Xifeng loess-paleosol sequence (Figure 5a).



401  
 402 **Figure 6:**  $^{14}\text{C}$  activity (expressed as  $\Delta^{14}\text{C}$ ; red circles) and  $\delta^{13}\text{C}$  (grey circles) of POC vs. SPM concentration for surface  
 403 samples from the Huanghe collected from 2011 to 2016 (average SPM concentration of surface samples in this study and  
 404 from Hu et al. (2015), Tao et al. (2015), Yu et al. (2019a), and Ge et al. (2020)). These paired dual carbon isotope data  
 405 corresponds to the group ‘SPM lower reaches’ in Figure 5. Straight lines correspond to best-fit logarithmic curves, and  
 406 shaded areas represent the 95% confidence interval.

407 The  $\text{N}/\text{C}_{\text{org}}$  ratio provides additional evidence for the significant contribution of loess-paleosol material to Huanghe  
 408 POC (Figure S6). Indeed, the  $\text{N}/\text{C}_{\text{org}}$  ratios of SPM collected in the lower reaches ranges from 0.10 to 0.23 (this study,  
 409 Ran et al., 2013; Yu et al., 2019a), whereas topsoils of the CLP are characterized by  $\text{N}/\text{C}_{\text{org}}$  lower than 0.14 (Liu and  
 410 Liu, 2017) and sedimentary rocks typically have very low  $\text{N}/\text{C}_{\text{org}}$  (Hilton et al., 2015). Soil OC input from the North  
 411 China Plain is also unlikely given its  $\text{N}/\text{C}_{\text{org}}$  of 0.10-0.13 (Shi et al., 2017). Therefore, all these possible sources cannot  
 412 explain the high  $\text{N}/\text{C}_{\text{org}}$  signatures of riverine SPM. In addition, the high turbidity of the Huanghe ( $> 600 \text{ mg/L}$ ) during  
 413 the sampling season is likely to inhibit *in-situ* primary production ( $\text{N}/\text{C}_{\text{org}} > 0.13$ ) (Zhang et al., 2013; Hu et al., 2015).  
 414 As a result, only soil OC from deep loess-paleosol horizons appears as a plausible supplier to downstream Huanghe  
 415 POC, given the high  $\text{N}/\text{C}_{\text{org}}$  ratios previously reported for various loess-paleosol sequences (Figure S6, Ning et al.,  
 416 2006).

417 Geomorphic processes in the CLP region support the erosion of deep soil horizons. There, gully erosion is thought to  
 418 be responsible for more than 80% of the total sediment yield in the CLP (He et al., 2006; Li et al., 2022). Gullies are  
 419 densely distributed and cover about 42% of the total area of the CLP and up to 60% in hilly regions (Huang and Ren,  
 420 2006; He et al., 2006). Nowadays, the well-developed gully geomorphic system of the CLP is characterized by gullies  
 421 with a depth of about 10 m on average and represents the most active vertical and regressive erosion of loess (Huang  
 422 and Ren, 2006). This incision process erodes all types of unconsolidated materials, including the loess-paleosol  
 423 sequence, underlying red clays, and colluvial deposits in the form of creeps, falls, and slides in the watershed (Zhu,  
 424 2012). From 1925 to 1981, the erosion rate of the CLP was  $6,318 \text{ t km}^{-2} \text{ yr}^{-1}$ , compared to  $10,770 \text{ t km}^{-2} \text{ yr}^{-1}$  in the  
 425 hilly and gully plateau (Li et al., 2022). While the CLP's erosion rate dropped to  $3,476 \text{ t km}^{-2} \text{ yr}^{-1}$  between 1982 and  
 426 2016, the rate in the hilly and gully plateau remained significantly high at  $6,146.5 \text{ t km}^{-2} \text{ yr}^{-1}$  (Li et al., 2022). All these

427 observations suggest that gully erosion can strongly impact the composition of riverine POC. As gully erosion is  
 428 sensitive to climate change and anthropogenic activities, soil dynamics in the Huanghe basin have been altered since  
 429 the mid-Holocene (He et al., 2006; Li et al., 2022). Notably, the strengthening of the East Asian Monsoon in coming  
 430 decades (Li et al., 2022; Xue et al., 2023) could potentially enhance this process. However, in recent years, soil and  
 431 water conservation and environmental rehabilitation campaigns (Wang et al., 2007) largely contributed to the  
 432 reduction of SPM export by the Huanghe with a transfer to the estuary of 10.6 Mt in 2016, which is one order of  
 433 magnitude lower than the annual sediment flux measured in 2013 (172.8 Mt) and two orders or magnitude lower  
 434 compared to the flux of the 1950s (*ca.* 1,340 Mt; Wang et al., 2015). This sediment load reduction is consistent with  
 435 the weakened erosion rate observed in the CLP, such modifications should thus have drastically inhibited the OC  
 436 mobilization from the CLP and the POC export by the Huanghe.

### 437 5.2.2 POC source determination and end member apportionment

438 Considering the SPM geochemistry and the basin characteristics, three terrestrial sources can be identified as necessary  
 439 to form the composition of the Huanghe POC at the Luokou cross-section. As discussed in Section 5.2.1 and shown  
 440 in Figure 5a, two of these sources are (a) topsoil-derived OC ( $OC_{ts}$ ) and (b) OC from deeper horizons of the loess-  
 441 paleosol sequence ( $OC_{lps}$ ) excluding topsoil. In addition, at the Luokou cross-section, bed OC shows lower  $F_m$  and  
 442  $\delta^{13}C$  values compared to that of SPM, suggesting a significant contribution of (c) rock-derived OC from erosion in the  
 443 middle reaches ( $OC_{petro}$ ).

444 We adopted a Bayesian Monte-Carlo model to reconstruct source apportionment based on the mass balance of carbon  
 445 isotopes ( $\delta^{13}C$  and  $\Delta^{14}C$ ) of our three defined end members (Section 3.3, Table. 2, Appendix A). The mixing space  
 446 showing the geometric area between three end members is shown in Figure S7. Modeling results are shown in Figure  
 447 7 as relative contributions (Figure 7a) and weight percentage (Figure 7b) of  $OC_{ts}$ ,  $OC_{lps}$ , and  $OC_{petro}$  (Table S2). The  
 448 contribution of  $OC_{petro}$  to total Huanghe POC at Luokou varies between 10.1% and 13.9% in the cross-section, which  
 449 is higher than the contribution calculated for in the two fine SPM samples (avg.  $9.1 \pm 0.3\%$ ) and much smaller than  
 450 for the bed sediment sample ( $72.2 \pm 10\%$ ). The inferred  $OC_{petro}$  concentration in the sediment is remarkably uniform  
 451 in the cross-section, representing 0.04% of SPM (Figure 7b). This result is consistent with the OC contents of  
 452 midstream sedimentary rocks at  $0.09 \pm 0.08\%$  (Qu et al., 2020). In addition, these findings imply that  $OC_{petro}$   
 453 concentration does not depend on particle size and confirm previous findings of  $OC_{petro}$  being present in a range of  
 454 clastic particles or as discrete particles (Galy et al., 2008a; Bouchez et al., 2014). In other words, the rock-derived OC  
 455 has a relatively invariant contribution with depth (Galy et al., 2008a; Bouchez et al., 2014), meaning that biospheric  
 456 OC exerts a first-order control on POC content and isotopic variations throughout the cross-section.

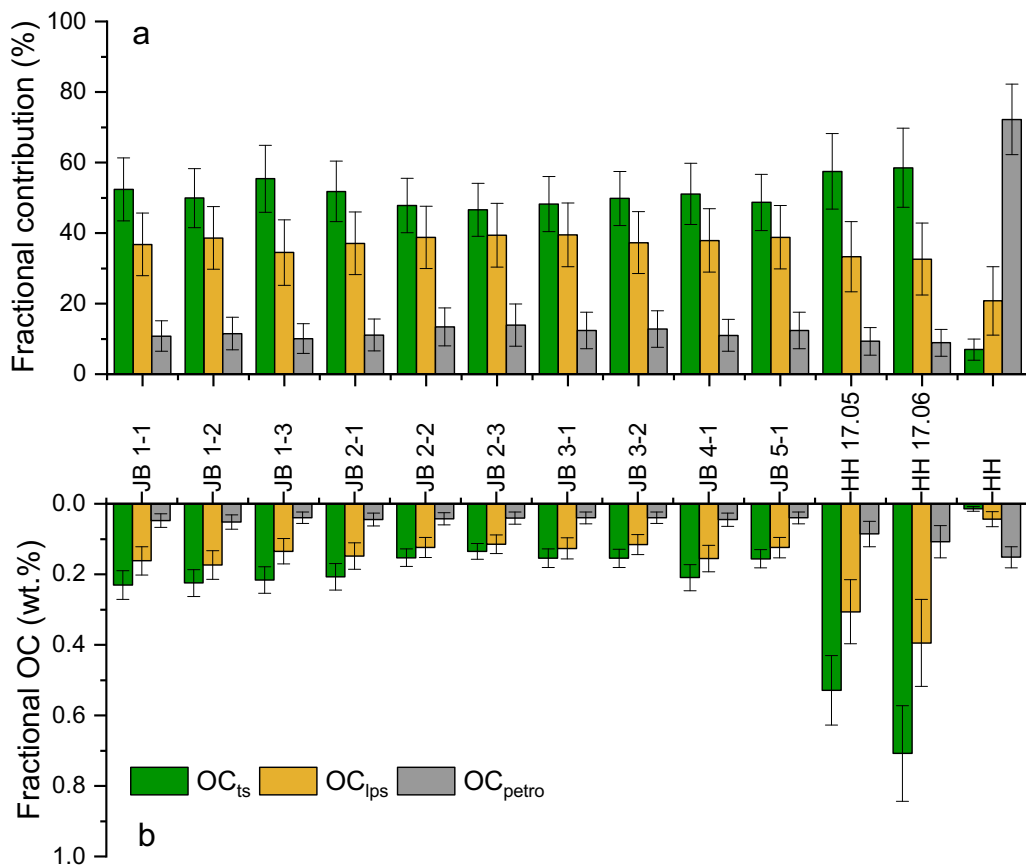
457 **Table 2: Summary of  $\delta^{13}C$  and  $\Delta^{14}C$  of source end members for POC in the Huanghe.**

End member	$\delta^{13}C$	$\Delta^{14}C$
$OC_{ts}$	$-24.8 \pm 1.9\%$	$-90 \pm 130\%$
$OC_{lps}$	$-22.7 \pm 1.0\%$	$-610 \pm 390\%$
$OC_{petro}$	$-28.1 \pm 1.5\%$	$-1000\%$

458 At the study cross-section,  $OC_{ts}$  and  $OC_{lps}$  contribute 46.6%-55.4% and 34.5%-39.5% to the total POC, respectively  
 459 (Figure 7a). The sum of these two components can be considered as  $OC_{bio}$ , which is  $88.0 \pm 1.3\%$ . The corresponding



460 OC<sub>bio</sub> content of sediment is quite variable, ranging from 0.25% (sample JB 2-3) to 0.40% (sample JB 1-2), and  
 461 generally decreases from the river surface to the bottom. Given the rather invariant OC<sub>petro</sub> concentration in the  
 462 sediment, there are thus marked heterogeneities of POC provenance in the cross-section. For instance, POC  
 463 transported close to the right bank and in the finer SPM samples show a higher contribution from OC<sub>bio</sub>. From the  
 464 knowledge of the relative contributions of OC<sub>ts</sub> and OC<sub>lps</sub> and their corresponding <sup>14</sup>C activity, the Fm values for the  
 465 bulk OC<sub>bio</sub> can be estimated based on mass balance. The modeled radiocarbon activity of OC<sub>bio</sub> varies from 0.64 to  
 466 0.75, corresponding to 3,570 to 2,300 <sup>14</sup>C yrs. In summary, our results support the first-order control of OC<sub>bio</sub>  
 467 abundance on POC content and age in the Huanghe.



468 **Figure 7: (a) Relative contributions of the three different sources of Huanghe POC, (b) fractional OC weight percentage**  
 469 **Huanghe POC at the Luokou cross-section, as inferred from a mixing model. OC<sub>ts</sub> is the topsoil-derived OC, OC<sub>lps</sub>**  
 470 **represents the loess-paleosol sequence OC excluding topsoil, and OC<sub>petro</sub> is the rock-derived OC eroded from the Huanghe**  
 471 **middle reaches.**  
 472

473 Applying the same mixing model to previously published Huanghe POC data (2011-2016, Table S1) shows (1)  
 474 dominance of the OC<sub>bio</sub> contribution to POC, (2) variable relative mixing proportions of OC<sub>ts</sub> and OC<sub>lps</sub>; (3) a wide  
 475 range of <sup>14</sup>C age for OC<sub>bio</sub> (from 1,779 to 8,325 yrs). In particular, OC<sub>ts</sub> and OC<sub>lps</sub> contributed 28%-35% and 53%-  
 476 63% to POC collected in 2013 (Hu et al., 2015), leading to 75-89% of OC<sub>bio</sub>. Yu et al. (2019a) estimated that OC<sub>bio</sub>  
 477 contributed 63%-81% to the lower Huanghe POC (2015-2016) using a different mixing model. Using their data in our  
 478 mixing model results in a higher OC<sub>bio</sub> contribution of 88%-91%, consisting of 43%-55% for OC<sub>ts</sub> and 36%-46% for  
 479 OC<sub>lps</sub>. The small difference in source contribution mainly results from the fact that old OC<sub>bio</sub> from loess-paleosol

480 sequences was not considered in Yu et al. (2019a), and from the different isotopic signatures chosen for the POC  
481 endmembers. However, both estimates ignore the possible presence of rock-derived OC in soils. In any case, our  
482 results suggest that the Huanghe transports more OC<sub>bio</sub>-derived POC than previously thought, with more aged, soil-  
483 derived OC.

484 It is worth noticing that these calculations suggest that the OC<sub>lps</sub> fraction in the Huanghe was significantly higher in  
485 2013 than in 2016. As most Huanghe sediments are derived from the CLP, higher physical erosion in the CLP should  
486 enhance supply of aged, refractory OC<sub>bio</sub> to the river system. Consequently, the decrease in sediment supply from the  
487 CLP initiated a few decades ago (Wang and Fu et al., 2016), which is likely to continue in the future, will probably  
488 lead to the reduction of the contribution of OC<sub>lps</sub> to total POC export from the Huanghe. This might have an impact  
489 on the burial efficiency of riverine POC on the continental margins, as OC<sub>ts</sub> is more labile than OC<sub>lps</sub>, and thus more  
490 prone to the remineralization process before burial. Moreover, decreasing erosion rate in the Huanghe basin will lead  
491 to decreasing sediment accumulation rate in the estuary, which potentially favors the oxidation of all POC components  
492 before burial (Blair and Aller, 2012). The time scale over which such effect could take place is yet unknown, as  
493 anthropogenic intervention is the primary reason for the sediment yield reduction, through afforestation and soil and  
494 water conservation measures in the CLP and reservoir operation in the middle reaches of the Huanghe. However, it is  
495 plausible that in response to decreased terrestrial physical erosion on the Loess Plateau over at least decadal timescales,  
496 an increased proportion of Huanghe POC will be oxidized before burial in the ocean, thereby leading to a weakened  
497 preservation efficiency for the terrestrial eroded POC.

### 498 **5.3 POC export by the Huanghe**

499 In the Huanghe, POC content varies both vertically and laterally throughout the cross-section (Figure 2). This spatial  
500 variability of both physical and chemical SPM characteristics must be considered when estimating integrated  
501 instantaneous POC concentration and flux (Section 3.4).

502 We calculate that (Text S1) at the sampling time (July 2016), the Huanghe at Luokou transported 1,075 kg/s of SPM  
503 for a water discharge of 731 m<sup>3</sup>/s, such that the spatially-integrated SPM concentration over the cross section (SPM<sub>int</sub>)  
504 was 1,472 mg/L, a value relatively close to the straightforward average concentration of our 10 samples (1,286 mg/L).  
505 The Luokou gauging station records a monthly SPM load of 1,826 kg/s in July 2016, and the daily average SPM load  
506 of 1,096 kg/s for a daily average water discharge of 643 m<sup>3</sup>/s on the 16<sup>th</sup> and 17<sup>th</sup> of July 2016 (method: three water  
507 samples collected at 0.5 m below the channel surface across the transect profile, data available at  
508 <http://www.yrcc.gov.cn>). Even though the latter estimate neglects the vertical heterogeneity within this relatively  
509 shallow river (< 5.0 m), estimates give similar results.

510 We further obtain an instantaneous POC flux of 3.69 kg/s, corresponding to a cross-section integrated average POC  
511 content (POC<sub>int</sub>%) of 0.34% when dividing this instantaneous POC flux by the instantaneous SPM load. Given the  
512 relatively homogenous distribution of OC<sub>petro</sub>, the instantaneous flux of OC<sub>petro</sub> was calculated by multiplying the  
513 average OC<sub>petro</sub> content by the instantaneous cross-section integrated SPM flux, yielding 0.44 ± 0.18 kg/s. The  
514 instantaneous OC<sub>bio</sub> flux was then calculated by subtracting the instantaneous flux of OC<sub>petro</sub> from the instantaneous  
515 POC flux, yielding 3.25 ± 0.20 kg/s. Assuming that our SPM samples are representative in terms of POC content

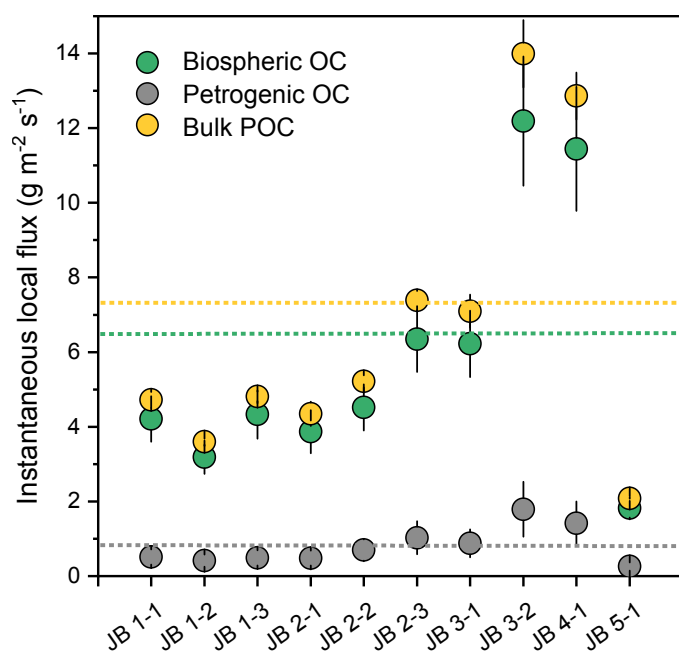
516 exported in July 2016, and taking the SPM flux of the gauging station for July, then the estimated fluxes of POC,  
517 OC<sub>bio</sub>, and OC<sub>petro</sub> for the flood period of July 2016 are 6.1, 5.4, and 0.7 kg/s, respectively. Taking POC<sub>int</sub> content for  
518 estimating the annual POC flux yields a value of 1.1 kg/s consisting of 1.0 and 0.1 kg/s for OC<sub>bio</sub> and OC<sub>petro</sub> fluxes,  
519 respectively. Note that these numbers are lower-bound estimates because POC content in Huanghe SPM collected  
520 during flood periods is generally the lowest (Ran et al., 2013). Taking the highest POC content 0.75% reported in the  
521 lower Huanghe in 2016 (Yu et al., 2019a), the estimated annual POC flux is 2.4 kg/s.

522 The above numbers present a sharp decrease compared to the estimated POC and OC<sub>bio</sub> fluxes transported by the  
523 Huanghe over the period 2008 to 2013. Galy et al. (2015) estimated an OC<sub>petro</sub> flux of 1.9 kg/s and an OC<sub>bio</sub> flux of  
524 11.4 kg/s from 2008 to 2012 (SPM flux: 3,655 kg/s, YRCC 2016), while Tao et al. (2018) reported an OC<sub>petro</sub> flux of  
525 5.8 kg/s and a similar OC<sub>bio</sub> flux of 12.6 kg/s from June 2012 to May 2013 (SPM flux: 5,723 kg/s, YRCC 2016).

526 We first note that previous estimates of POC flux in the Huanghe might be biased as these estimates neglect the  
527 variability over the cross-section (*e.g.*, Hu et al., 2015; Ran et al., 2013; Tao et al., 2015), SPM samples analyzed so  
528 far for the Huanghe were generally collected within the first 0.5 m below the surface, meaning that previous POC  
529 estimates did not consider the observed vertical and lateral POC heterogeneities and have thus misestimated POC  
530 sources and fluxes. Those estimates were calculated by multiplying an individual surface POC content by the  
531 corresponding monthly or weekly suspended sediment load, as provided by hydrological stations. Such estimates can  
532 be problematic because POC content in SPM generally decreases from top to bottom (Figure 2), resulting in biased  
533 surface-based estimates of fluxes (Bouchez et al., 2014). Using our cross-section data, we can estimate the bias in  
534 POC flux estimates when a single sample is used for such flux estimates, by multiplying depth-integrated sediment  
535 flux by the POC content of each sample. Such calculation shows different POC fluxes ranging from -15% to +30%  
536 compared to the depth-integrated estimate, which is mostly influenced by the variable POC content. Considering SPM  
537 collected at the channel surface, POC flux estimates using samples JB 1-1 and JB 2-1 are 28% and 15% higher,  
538 respectively, and are 6% and 5% lower using samples JB 3-1 and JB 5-1, respectively, than the depth-integrated  
539 estimate. This simple sensitivity analysis shows that channel surface sampling of SPM alone does not necessarily  
540 result in an overestimation of POC flux because of lateral heterogeneity, even though the POC content of SPM is  
541 generally higher at the surface than at the bottom (Figure 2). Consequently, and although accurate estimation of POC  
542 fluxes requires grain-size variations to be accounted for, the corresponding bias cannot explain the large difference  
543 between our estimates of Huanghe POC export for the year 2016 and previous estimates for preceding years. The SPM  
544 flux is 336 kg/s in 2016 and 762 kg/s over the period 2014 to 2016, which is one order of magnitude lower than values  
545 reported from 2008 to 2013 (YRCC 2016). The dramatic decrease in sediment load of the Huanghe (Wang and Fu et  
546 al., 2016) has most likely exerted a first-order control on the reduction in POC export from the Huanghe river system,  
547 and will probably continue to do so in the near future.

548 In the lower Huanghe, the POC content is very low and has small variance among different size fractions (Get et al.,  
549 2020), such that the POC flux is controlled by the SPM flux. In particular, it is worth noting that the Huanghe displays  
550 strong density stratification effects compared to other rivers (Moodie et al., 2022), with near-bed flow dominating the  
551 transport of SPM. In order to appraise how spatial and temporal variability in SPM flux could influence POC export,  
552 "local" POC loads can be calculated throughout the cross-section using the local water velocity, SPM concentration,

553 and POC content (Figure 8). In general, in the lower Huanghe more POC is transported near the riverbed and above  
 554 shallower bathymetry on the left side of the channel (except for profile JB 5). For instance, there is a nearly two-fold  
 555 increase in POC export from the surface to the bottom for the JB 2 and JB 3 profiles. The maximum local bulk POC  
 556 ( $14.0 \text{ gC m}^{-2} \text{ s}^{-1}$ ),  $\text{OC}_{\text{bio}}$  ( $12.2 \text{ gC m}^{-2} \text{ s}^{-1}$ ), and  $\text{OC}_{\text{petro}}$  export ( $1.8 \text{ gC m}^{-2} \text{ s}^{-1}$ ) are of sample JB 3-2, representing over  
 557 6 times the size of the corresponding minimum value (sample JB 5-1). This spatial pattern of POC load is almost the  
 558 reverse of the POC% variation over the cross-section, again stressing the importance of sediment river dynamics in  
 559 POC delivery. From these considerations, it could be anticipated that during the low-water season, when water velocity  
 560 is slower, near-bottom Huanghe SPM is deposited on the channel bed, withdrawing a significant fraction of the POC  
 561 export, as shown in other large rivers (Ke et al., 2022). This topic should be further examined in future research, in  
 562 order to systematically investigate the stratification of sediment and associated OC transport dynamics in lowland and  
 563 high-turbidity fluvial systems.



564  
 565 **Figure 8: Estimates of instantaneous “local” fluxes of Huanghe bulk POC,  $\text{OC}_{\text{bio}}$  and  $\text{OC}_{\text{petro}}$ , calculated for each sample of**  
 566 **the Luokou cross-section. The three dotted lines marked in orange, green, and grey represent the corresponding**  
 567 **instantaneous, cross-section integrated fluxes. The error bar represents 1 standard deviation.**

568 Interestingly, anthropogenic activities may have antagonistic effects on POC export. Deforestation, agriculture, and  
 569 mining have considerably enhanced the sediment yield from the CLP since the mid-Holocene (He et al., 2006) while  
 570 the construction of large dams, soil and water conservation measures, and afforestation has considerably reduced the  
 571 sediment yield since the 1950s (Wang and Fu et al., 2016; Wang et al., 2007; Syvitski et al., 2005). Yet the Huanghe  
 572 exports substantial  $\text{OC}_{\text{bio}}$  and  $\text{OC}_{\text{petro}}$  with a significantly higher burial efficiency (avg. ca. 42%; Sun et al., 2018) than  
 573 other large fluvial systems entering passive continental margins, such as the Changjiang, Amazon, and Mississippi  
 574 (Blair and Aller, 2012). It is reported that aged soil OC is nearly fully preserved in continental margins and that  $\text{OC}_{\text{petro}}$   
 575 has a ca. 70% burial efficiency (Tao et al., 2016). However, the contribution of the Huanghe OC burial to the global  
 576 C sink is likely to be lower in the future as the consequence of 1) sharp decrease in SPM and POC export due to

577 weakened physical erosion in the CLP; 2) reduced sediment accumulation rate favoring OC remineralization in  
578 estuaries (Blair and Aller, 2012; Walling and Fan, 2003; Milliman and Farnsworth, 2011; Galy et al., 2015).

## 579 **6 Conclusions**

580 In this contribution, we present the first detailed study of particulate organic carbon (POC) over a complete river cross-  
581 section of the Huanghe, providing new perspectives on the transport mode, source, and instantaneous fluxes of POC  
582 in this highly turbid large river.

583 At the scale of a cross-section, physical and chemical properties of SPM are heterogeneous both vertically and  
584 laterally, a feature that is mainly controlled by bathymetry and hydrodynamic sorting. Resuspension of bed sediment  
585 and local erosion of the right bank together impact the suspended POC composition at the sampled location. This  
586 spatial heterogeneity shows that near-bottom SPM plays a dominant role in the delivery of OC<sub>bio</sub> (topsoil and deep  
587 soil OC combined) and OC<sub>petro</sub>. Despite a relatively shallow river channel (< 5.0 m) and narrow width (< 200 m), we  
588 show how the heterogeneity of POC transport over a cross-section needs to be considered in constraining POC  
589 transport mode and estimating POC fluxes.

590 Despite its millennial age, POC in the Huanghe is dominated by OC<sub>bio</sub> with a contribution of  $88.0 \pm 1.3$  %. OC<sub>petro</sub>  
591 content in SPM is relatively homogeneous (0.04% - 0.05%) over the cross-section, indicating that the variability in  
592 bulk POC age is mainly controlled by the variability in OC<sub>bio</sub> content, especially in the finest SPM fraction. OC<sub>bio</sub> ages  
593 deduced from the application of a mixing model to previously published data (record period 2011-2016) are highly  
594 variable, ranging from 1,779 to 8,325 <sup>14</sup>C yrs. We interpret this feature as resulting from the erosion of deep horizons  
595 by gully systems in the loess-paleosol sequences containing <sup>14</sup>C-dead OC<sub>bio</sub>. Enhanced erosion of deep loess-paleosol  
596 horizons mobilizes aged and refractory OC to the ocean, with high burial efficiency on the passive margin. The erosion  
597 of loess-paleosol horizons is thus an efficient process of CO<sub>2</sub> burial. However, the construction of large dams has  
598 drastically affected the sediment load of the Huanghe system and retains substantial quantities of sediments that were  
599 previously exported to the ocean. Future work is needed to further quantify how these anthropogenic modifications  
600 alter POC composition and transport, by conducting comprehensive cross-section sampling campaigns over extended  
601 time series upstream and downstream from dams.

## 602 **Appendix A**

603 Fluvial POC delivered in the Huanghe POC could originate from three terrestrial sources (Table. 2). As topsoil  
604 typically contains recently photosynthesized OC<sub>bio</sub>, we used a  $\delta^{13}\text{C}$  value of  $-24.8 \pm 1.9\text{‰}$  (n=166) according to the  
605 subsurface soil OC values measured across the Huanghe basin (Rao et al., 2017). Over the sampled cross-section, the  
606 depleted <sup>13</sup>C values indicate the dominant and almost exclusive input of C3 plant-derived material to the Huanghe  
607 POC in the lower reaches. Based on <sup>14</sup>C (Liu et al., 2012) and <sup>10</sup>Be (Zhou et al., 2010) dating of < 10 cm-deep soil  
608 horizons in the Huanghe Basin, the average age of topsoil was chosen as being younger than 2,000 yrs (*i.e.*,  $\Delta^{14}\text{C} >$   
609  $-220\text{‰}$ ). As for the topsoil end member includes modern biospheric material ( $\Delta^{14}\text{C}$  around 40‰, Hua et al., 2013),  
610 we assigned a  $\Delta^{14}\text{C}$  value of  $-90 \pm 130\text{‰}$  (Fm =  $0.91 \pm 0.13$ ). This range also includes the range of  $\Delta^{14}\text{C}$  values of

611 pre-aged soil OC indicated by the long-chain n-C<sub>24+26+28</sub> alkanols of the Huanghe POC reported by Tao et al. (2015)  
612 and Yu et al. (2019a). Their results show consistent POC  $\Delta^{14}\text{C}$  values in the lower reaches of  $-204 \pm 20\text{‰}$  ( $F_m = 0.80$   
613  $\pm 0.03$ ,  $n=7$ ) from June 2015 to May 2016 and  $-219 \pm 33\text{‰}$  ( $F_m = 0.79 \pm 0.04$ ,  $n=4$ ) at Kenli and of  $-198 \pm 15\text{‰}$  ( $F_m$   
614  $= 0.81 \pm 0.02$ ,  $n=6$ ) from June 2015 to April 2016 at Huayuankou (Tao et al., 2015; Yu et al., 2019a).

615 The second end member should be characterized by aged and refractory OC from the loess-paleosol sequence  
616 excluding topsoil (upper 10 m) of the CLP. Radiocarbon dating has an upper age limit of around 50,000 yrs, age above  
617 which  $F_m$  is equal to 0. However, radiocarbon-free OC spanning from 50,000 to 100,000 yrs must still be considered  
618 as OC<sub>bio</sub> in the long-term carbon cycle. Here, we name this ignored OC as the “dormant” OC, without which the OC<sub>bio</sub>  
619 (*i.e.*, less than 100,000 yrs old) would be underestimated to some extent because the radiocarbon-free OC would be  
620 misinterpreted as having a petrogenic origin. To consider this “dormant” OC, a  $\delta^{13}\text{C}$  values of  $-22.7 \pm 1.0\text{‰}$  ( $n=34$ ,  
621 Ning et al., 2006) and a  $\Delta^{14}\text{C}$  values of  $-610 \pm 390\text{‰}$  ( $F_m$ ,  $0.39 \pm 0.39$ ) were adopted based on an average of values  
622 over the whole loess-paleosol sequence. Although radiocarbon-free (*i.e.*, older than 100,000 yrs) OC overlaps with  
623 this end member, such old soil organic carbon is probably not mobilized as modern gully erosion mainly concerns the  
624 upper 10 m of the loess-paleosol sequences, where soil OC<sub>bio</sub> is assumed to be significantly younger comparatively  
625 (Figure 5).

626 Rock-derived OC from the QTP and the CLP, as well as kerogen from oil-gas fields from the Ordos Basin,  
627 were all considered to be possible contributors to the OC<sub>petro</sub> endmember. The  $\delta^{13}\text{C}$  of OC<sub>petro</sub> greatly varies between  
628 the QTP ( $-21.2 \pm 1.2\text{‰}$ ,  $n=11$ , Liu et al., 2007) and the CLP ( $-26.8 \pm 0.5\text{‰}$ ,  $n=8$ , Qu et al., 2020). However, most of  
629 the sediments eroded from the QTP are not transferred to the lower reaches as they remain trapped in the CLP and the  
630 western Mu Us desert (Nie et al., 2015; Licht et al., 2016; Pan et al., 2016). In addition, the construction of large dams  
631 in the upper reaches has considerably reduced the transfer of solid materials downstream (Wang et al., 2007).  
632 Therefore, rock-derived OC inherited from the denudation of the QTP region is not further considered. Kerogen from  
633 the oil-gas fields of the Ordos Basin in the CLP region (Figure 1) has  $\delta^{13}\text{C}$  values of  $-29.2 \pm 0.9\text{‰}$  ( $n=10$ , Guo et al.,  
634 2014). Taking these constraints together, we consider a  $\delta^{13}\text{C}$  value of  $-28.1 \pm 1.5\text{‰}$  ( $n=18$ ) for the OC<sub>petro</sub> end member,  
635 and a  $\Delta^{14}\text{C}$  value of  $-1000\text{‰}$  ( $F_m = 0$ ) by definition.

## 636 Key Points

- 637  Bank erosion in lower Huanghe provides recent organic carbon to fluvial transport, altering the particulate  
638 organic carbon transport over a river channel cross-section;
- 639  Erosion of deep soil horizons of the loess-paleosol sequence contributes radiocarbon-dead organic carbon  
640 from the biosphere to the Huanghe;
- 641  Channel-bottom transport in the Huanghe is the primary process of exporting fluvial particulate organic  
642 carbon to the estuary.

## 643 Data availability

644 All datasets are included in the paper and the supplementary materials.

645 **Author contributions**

646 DC, JB, CQ, and YK conceptualized the study. DC, JB, YK, MM, and BC determined the methodology. HC and JC  
647 collected the sediment samples. YK, MM, and AN assisted with elemental and isotopic carbon analysis. DC and CQ  
648 supervised the work. KY performed data analysis and wrote the original draft, and all authors contributed to the review  
649 and editing of the paper.

650 **Competing interests**

651 We declare there is no competing interest.

652 **Acknowledgments**

653 We thank Yulong Liu and Shengliu Yuan for their help during sampling and filtering. We also thank François Thil  
654 and Nadine Tissenerat for invaluable help when running the ECHoMICADAS, and Pierre Barré for use of the  
655 Beckman Coulter's LS 13 320 for particle size analysis at École normale supérieure.

656 **Financial support**

657 This study was financially supported by the Agence Nationale de la Recherche (ANR) SEDIMAN (Grant ANR-15-  
658 CE01-0012), the National Natural Science Foundation of China (NSFC), grants 41561134017, 41625012, and the  
659 China Scholarship Council (CSC) to Yutian Ke (No.201706180008).

660 **References**

- 661 Baronas, J. J., Stevenson, E. I., Hackney, C. R., Darby, S. E., Bickle, M. J., Hilton, R. G., Larkin, C. S., Parsons, D.  
662 R., Myo Khaing, A., and Tipper, E. T.: Integrating Suspended Sediment Flux in Large Alluvial River Channels:  
663 Application of a Synoptic Rouse-Based Model to the Irrawaddy and Salween Rivers, *Journal of Geophysical Research:*  
664 *Earth Surface*, 125, <https://doi.org/10.1029/2020jf005554>, 2020.
- 665 Bianchi, T. S.: The role of terrestrially derived organic carbon in the coastal ocean: A changing paradigm and the  
666 priming effect, *Proceedings of the National Academy of Sciences*, 108, 19473–19481,  
667 <https://doi.org/10.1073/pnas.1017982108>, 2011.
- 668 Bird, A., Stevens, T., Rittner, M., Vermeesch, P., Carter, A., Andò, S., Garzanti, E., Lu, H., Nie, J., Zeng, L., Zhang,  
669 H., and Xu, Z.: Quaternary dust source variation across the Chinese Loess Plateau, *Palaeogeography,*  
670 *Palaeoclimatology, Palaeoecology*, 435, 254–264, <https://doi.org/10.1016/j.palaeo.2015.06.024>, 2015.
- 671 Blair, N. E. and Aller, R. C.: The Fate of Terrestrial Organic Carbon in the Marine Environment, *Annual Review of*  
672 *Marine Science*, 4, 401–423, <https://doi.org/10.1146/annurev-marine-120709-142717>, 2012.
- 673 Blair, N. E., Leithold, E. L., Brackley, H., Trustrum, N., Page, M., and Childress, L.: Terrestrial sources and export of  
674 particulate organic carbon in the Waipaoa sedimentary system: Problems, progress and processes, *Marine Geology*,  
675 270, 108–118, <https://doi.org/10.1016/j.margeo.2009.10.016>, 2010.
- 676 Bouchez, J., Galy, V., Hilton, R. G., Gaillardet, J., Moreira-Turcq, P., Pérez, M. A., France-Lanord, C., and Maurice,  
677 L.: Source, transport and fluxes of Amazon River particulate organic carbon: Insights from river sediment depth-  
678 profiles, *Geochimica et Cosmochimica Acta*, 133, 280–298, <https://doi.org/10.1016/j.gca.2014.02.032>, 2014.
- 679 Bouchez, J., Gaillardet, J., France-Lanord, C., Maurice, L., and Dutra-Maia, P.: Grain size control of river suspended  
680 sediment geochemistry: Clues from Amazon River depth profiles, *Geochemistry, Geophysics, Geosystems*, 12, n/a-  
681 n/a, <https://doi.org/10.1029/2010gc003380>, 2011a.

682 Bouchez, J., Lupker, M., Gaillardet, J., France-Lanord, C., and Maurice, L.: How important is it to integrate riverine  
683 suspended sediment chemical composition with depth? Clues from Amazon River depth-profiles, *Geochimica et*  
684 *Cosmochimica Acta*, 75, 6955–6970, <https://doi.org/10.1016/j.gca.2011.08.038>, 2011.

685 Carignan, J., Hild, P., Mevelle, G., Morel, J., and Yeghicheyan, D.: Routine Analyses of Trace Elements in Geological  
686 Samples using Flow Injection and Low Pressure On-Line Liquid Chromatography Coupled to ICP-MS: A Study of  
687 Geochemical Reference Materials BR, DR-N, UB-N, AN-G and GH, *Geostandards Newsletter*, 25, 187–198,  
688 <https://doi.org/10.1111/j.1751-908X.2001.tb00595.x>, 2001.

689 Cauwet, G. and Mackenzie, F. T.: Carbon inputs and distribution in estuaries of turbid rivers: the Yang Tze and Yellow  
690 rivers (China), *Marine Chemistry*, 43, 235–246, [https://doi.org/10.1016/0304-4203\(93\)90229-h](https://doi.org/10.1016/0304-4203(93)90229-h), 1993.

691 Cheng, P., Burr, G. S., Zhou, W., Chen, N., Hou, Y., Du, H., Fu, Y., and Lu, X.: The deficiency of organic matter 14C  
692 dating in Chinese Loess-paleosol sample, *Quaternary Geochronology*, 56, 101051,  
693 <https://doi.org/10.1016/j.quageo.2019.101051>, 2020.

694 Curry, K. J., Bennett, R. H., Mayer, L. M., Curry, A., Abril, M., Biesiot, P. M., and Hulbert, M. H.: Direct visualization  
695 of clay microfabric signatures driving organic matter preservation in fine-grained sediment, *Geochimica et*  
696 *Cosmochimica Acta*, 71, 1709–1720, <https://doi.org/10.1016/j.gca.2007.01.009>, 2007.

697 Dellinger, M., Gaillardet, J., Bouchez, J., Calmels, D., Galy, V., Hilton, R. G., Louvat, P., and France-Lanord, C.:  
698 Lithium isotopes in large rivers reveal the cannibalistic nature of modern continental weathering and erosion, *Earth*  
699 *and Planetary Science Letters*, 401, 359–372, <https://doi.org/10.1016/j.epsl.2014.05.061>, 2014.

700 Feng, X., Feakins, S. J., Liu, Z., Ponton, C., Wang, R. Z., Karkabi, E., Galy, V., Berelson, W. M., Nottingham, A.  
701 T., Meir, P., and West, A. J.: Source to sink: Evolution of lignin composition in the Madre de Dios River system  
702 with connection to the Amazon basin and offshore, *Journal of Geophysical Research: Biogeosciences*, 121, 1316–  
703 1338, <https://doi.org/10.1002/2016JG003323>, 2016.

704 Freymond, C. V., Lupker, M., Peterse, F., Haghypour, N., Wacker, L., Filip, F., Giosan, L., and Eglinton, T. I.:  
705 Constraining Instantaneous Fluxes and Integrated Compositions of Fluvially Discharged Organic Matter, *Geochem*  
706 *Geophys Geosy*, 19, 2453–2462, <https://doi.org/10.1029/2018gc007539>, 2018.

707 Gaillardet, J., Dupré, B., Louvat, P., and Allègre, C. J.: Global silicate weathering and CO<sub>2</sub> consumption rates deduced  
708 from the chemistry of large rivers, *Chemical Geology*, 159, 3–30, [https://doi.org/10.1016/s0009-2541\(99\)00031-5](https://doi.org/10.1016/s0009-2541(99)00031-5),  
709 1999.

710 Galy, V. and Eglinton, T.: Protracted storage of biospheric carbon in the Ganges–Brahmaputra basin, *Nature Geosci*,  
711 4, 843–847, <https://doi.org/10.1038/ngeo1293>, 2011.

712 Galy, V., Beyssac, O., France-Lanord, C., and Eglinton, T.: Recycling of graphite during Himalayan erosion: a  
713 geological stabilization of carbon in the crust, *Science*, 322, 943–5, <https://doi.org/10.1126/science.1161408>, 2008a.

714 Galy, V., France-Lanord, C., and Lartiges, B.: Loading and fate of particulate organic carbon from the Himalaya to  
715 the Ganga–Brahmaputra delta, *Geochimica et Cosmochimica Acta*, 72, 1767–1787,  
716 <https://doi.org/10.1016/j.gca.2008.01.027>, 2008b.

717 Galy, V., France-Lanord, C., Beyssac, O., Faure, P., Kudrass, H., and Palhol, F.: Efficient organic carbon burial in the  
718 Bengal fan sustained by the Himalayan erosional system, *Nature*, 450, 407–10, <https://doi.org/10.1038/nature06273>,  
719 2007.

720 Galy, V., Peucker-Ehrenbrink, B., and Eglinton, T.: Global carbon export from the terrestrial biosphere controlled by  
721 erosion, *Nature*, 521, 204–7, <https://doi.org/10.1038/nature14400>, 2015.

722 Garzanti, E., Andò, S., France-Lanord, C., Vezzoli, G., Censi, P., Galy, V., and Najman, Y.: Mineralogical and  
723 chemical variability of fluvial sediments: 1. Bedload sand (Ganga–Brahmaputra, Bangladesh), *Earth and Planetary*  
724 *Science Letters*, 299, 368–381, <https://doi.org/10.1016/j.epsl.2010.09.017>, 2010.

725 Garcia, M.: *Sedimentation Engineering*, American Society of Civil Engineers, (pp. 21-163)  
726 <https://doi.org/10.1061/9780784408148>, 2008.

727 Ge, T., Xue, Y., Jiang, X., Zou, L., and Wang, X.: Sources and radiocarbon ages of organic carbon in different grain  
728 size fractions of Yellow River-transported particles and coastal sediments, *Chemical Geology*, 534, 119452,  
729 <https://doi.org/10.1016/j.chemgeo.2019.119452>, 2020.

730 Gu, Z., Duan, X., Shi, Y., Li, Y., and Pan, X.: Spatiotemporal variation in vegetation coverage and its response to  
731 climatic factors in the Red River Basin, China, *Ecological Indicators*, 93, 54–64,  
732 <https://doi.org/10.1016/j.ecolind.2018.04.033>, 2018.

733 Guo, H., Jia, W., Peng, P., Lei, Y., Luo, X., Cheng, M., Wang, X., Zhang, L., and Jiang, C.: The composition and its  
734 impact on the methane sorption of lacustrine shales from the Upper Triassic Yanchang Formation, Ordos Basin, China,  
735 *Marine and Petroleum Geology*, 57, 509–520, <https://doi.org/10.1016/j.marpetgeo.2014.05.010>, 2014.



736 Guo, K., Zou, T., Jiang, D., Tang, C., and Zhang, H.: Variability of Yellow River turbid plume detected with satellite  
737 remote sensing during water-sediment regulation, *Continental Shelf Research*, 135, 74–85,  
738 <https://doi.org/10.1016/j.csr.2017.01.017>, 2017.

739 Guo, L., Ping, C.-L., and Macdonald, R. W.: Mobilization pathways of organic carbon from permafrost to arctic rivers  
740 in a changing climate, *Geophysical Research Letters*, 34, <https://doi.org/10.1029/2007GL030689>, 2007.

741 Guo, Z. T., Ruddiman, W. F., Hao, Q. Z., Wu, H. B., Qiao, Y. S., Zhu, R. X., Peng, S. Z., Wei, J. J., Yuan, B. Y., and  
742 Liu, T. S.: Onset of Asian desertification by 22 Myr ago inferred from loess deposits in China, *Nature*, 416, 159–163,  
743 <https://doi.org/10.1038/416159a>, 2002.

744 Hatté, C., Arnold, M., Dapoigny, A., Daux, V., Delibrias, G., Boisguezeneuc, D. D., Fontugne, M., Gauthier, C.,  
745 Guillier, M.-T., Jacob, J., Jaudon, M., Kaltnecker, É., Labeyrie, J., Noury, C., Paterne, M., Pierre, M., Phouybanhdyt,  
746 B., Poupeau, J.-J., Tannau, J.-F., Thil, F., Tisnérat-Laborde, N., and Valladas, H.: Radiocarbon dating on  
747 ECHOMICADAS, LSCE, Gif-Sur-Yvette, France: new and updated chemical procedures, *Radiocarbon*, 1–16,  
748 <https://doi.org/10.1017/RDC.2023.46>, 2023.

749 He, X., Zhou, J., Zhang, X., and Tang, K.: Soil erosion response to climatic change and human activity during the  
750 Quaternary on the Loess Plateau, China, *Reg Environ Change*, 6, 62–70, <https://doi.org/10.1007/s10113-005-0004-7>,  
751 2006.

752 Hemingway, J. D., Hilton, R. G., Hovius, N., Eglinton, T. I., Haghypour, N., Wacker, L., Chen, M. C., and Galy, V.  
753 V.: Microbial oxidation of lithospheric organic carbon in rapidly eroding tropical mountain soils, *Science*, 360, 209–  
754 212, <https://doi.org/10.1126/science.aao6463>, 2018.

755 Hemingway, J. D., Rothman, D. H., Grant, K. E., Rosengard, S. Z., Eglinton, T. I., Derry, L. A., and Galy, V. V.:  
756 Mineral protection regulates long-term global preservation of natural organic carbon, *Nature*, 570, 228–231,  
757 <https://doi.org/10.1038/s41586-019-1280-6>, 2019.

758 Hilton, R. G., Gaillardet, J., Calmels, D., and Birck, J.-L.: Geological respiration of a mountain belt revealed by the  
759 trace element rhenium, *Earth and Planetary Science Letters*, 403, 27–36, <https://doi.org/10.1016/j.epsl.2014.06.021>,  
760 2014.

761 Hilton, R. G., Galy, A., Hovius, N., Horng, M.-J., and Chen, H.: Efficient transport of fossil organic carbon to the  
762 ocean by steep mountain rivers: An orogenic carbon sequestration mechanism, *Geology*, 39, 71–74,  
763 <https://doi.org/10.1130/g31352.1>, 2011.

764 Hilton, R. G., Galy, V., Gaillardet, J., Dellinger, M., Bryant, C., O'Regan, M., Grocke, D. R., Coxall, H., Bouchez, J.,  
765 and Calmels, D.: Erosion of organic carbon in the Arctic as a geological carbon dioxide sink, *Nature*, 524, 84–7,  
766 <https://doi.org/10.1038/nature14653>, 2015.

767 Hu, B., Li, J., Bi, N., Wang, H., Wei, H., Zhao, J., Xie, L., Zou, L., Cui, R., Li, S., Liu, M., and Li, G.: Effect of  
768 human-controlled hydrological regime on the source, transport, and flux of particulate organic carbon from the lower  
769 Huanghe (Yellow River), *Earth Surface Processes and Landforms*, 40, 1029–1042, <https://doi.org/10.1002/esp.3702>,  
770 2015.

771 Hua, Q., Barbetti, M., and Rakowski, A. Z.: Atmospheric Radiocarbon for the Period 1950–2010, *Radiocarbon*, 55,  
772 2059–2072, [https://doi.org/10.2458/azu\\_js\\_rc.v55i2.16177](https://doi.org/10.2458/azu_js_rc.v55i2.16177), 2013.

773 Huang, C. C., and Ren, Z: Fluvial erosion and the formation of gully systems over the Chinese Loess Plateau, *WSEAS*  
774 *Transactions on Environment and Development*, 2(2), 141-145, 2006.

775 Jahn, B., Gallet, S., and Han, J.: Geochemistry of the Xining, Xifeng and Jixian sections, Loess Plateau of China:  
776 eolian dust provenance and paleosol evolution during the last 140 ka, *Chemical Geology*, 178, 71–94,  
777 [https://doi.org/10.1016/S0009-2541\(00\)00430-7](https://doi.org/10.1016/S0009-2541(00)00430-7), 2001.

778 Ke, Y., Calmels, D., Bouchez, J., and Quantin, C.: MODern River archivEs of Particulate Organic Carbon:  
779 MOREPOC, *Earth System Science Data Discussions*, 1–19, <https://doi.org/10.5194/essd-2022-161>, 2022.

780 Keil, R. G., Mayer, L. M., Quay, P. D., Richey, J. E., and Hedges, J. I.: Loss of organic matter from riverine particles  
781 in deltas, *Geochimica et Cosmochimica Acta*, 61, 1507–1511, [https://doi.org/10.1016/S0016-7037\(97\)00044-6](https://doi.org/10.1016/S0016-7037(97)00044-6), 1997.

782 Gen Li, X. T. W., Zhongfang Yang, Changping Mao, A. Joshua West, Junfeng Ji: Dam-triggered organic carbon  
783 sequestration makes the Changjiang (Yangtze) river basin (China) a significant carbon sink, *Journal of Geophysical*  
784 *Research: Biogeosciences*, 2015.

785 Li, P., Chen, J., Zhao, G., Holden, J., Liu, B., Chan, F. K. S., Hu, J., Wu, P., and Mu, X.: Determining the drivers and  
786 rates of soil erosion on the Loess Plateau since 1901, *Science of The Total Environment*, 823, 153674,  
787 <https://doi.org/10.1016/j.scitotenv.2022.153674>, 2022.

788 Licht, A., Pullen, A., Kapp, P., Abell, J., and Giesler, N.: Eolian cannibalism: Reworked loess and fluvial sediment as  
789 the main sources of the Chinese Loess Plateau, *GSA Bulletin*, 128, 944–956, <https://doi.org/10.1130/B31375.1>, 2016.

790 Liu, G., Xu, W., Zhang, Q., & Xia, Z. : Holocene Soil Chronofunctions, Luochuan, Chinese Loess Plateau.  
791 *Radiometric Dating*, 41, 2012.

792 Liu, J. and Liu, W.: Soil nitrogen isotopic composition of the Xifeng loess-paleosol sequence and its potential for use  
793 as a paleoenvironmental proxy, *Quaternary International*, 440, 35–41, <https://doi.org/10.1016/j.quaint.2016.04.018>,  
794 2017.

795 Liu, W., Yang, H., Ning, Y., and An, Z.: Contribution of inherent organic carbon to the bulk  $\delta^{13}\text{C}$  signal in loess  
796 deposits from the arid western Chinese Loess Plateau, *Organic Geochemistry*, 38, 1571–1579,  
797 <https://doi.org/10.1016/j.orggeochem.2007.05.004>, 2007.

798 Ludwig, W., Probst, J.-L., and Kempe, S.: Predicting the oceanic input of organic carbon by continental erosion,  
799 *Global Biogeochemical Cycles*, 10, 23–41, <https://doi.org/10.1029/95gb02925>, 1996.

800 Mayorga, E., Aufdenkampe, A. K., Masiello, C. A., Krusche, A. V., Hedges, J. I., Quay, P. D., Richey, J. E., and  
801 Brown, T. A.: Young organic matter as a source of carbon dioxide outgassing from Amazonian rivers, *Nature*, 436,  
802 538–41, <https://doi.org/10.1038/nature03880>, 2005.

803 Milliman, J. D. and Farnsworth, K. L.: *River discharge to the coastal ocean: a global synthesis*, Cambridge University  
804 Press, 2011.

805 Milliman, J. D., Yun-Shan, Q., Mei-E, R., and Saito, Y.: Man's Influence on the Erosion and Transport of Sediment  
806 by Asian Rivers: The Yellow River (Huanghe) Example, *The Journal of Geology*, 95, 751–762,  
807 <https://doi.org/10.1086/629175>, 1987.

808 Moodie, A. J., Nittrouer, J. A., Ma, H., Carlson, B. N., Wang, Y., Lamb, M. P., and Parker, G.: Suspended Sediment-  
809 Induced Stratification Inferred From Concentration and Velocity Profile Measurements in the Lower Yellow River,  
810 China, *Water Resources Research*, 58, e2020WR027192, <https://doi.org/10.1029/2020WR027192>, 2022.

811 Moore, J. W., and Semmens, B. X.: Incorporating uncertainty and prior information into stable isotope mixing  
812 models. *Ecology Letters*, 11(5), 470–480, <https://doi.org/10.1111/j.1461-0248.2008.01163.x>, 2008.

813 Ning, Y., Liu, W., and An, Z.: Variation of soil  $\delta^{13}\text{C}$  values in Xifeng loess-paleosol sequence and its  
814 paleoenvironmental implication, *Chinese Sci Bull*, 51, 1350–1354, <https://doi.org/10.1007/s11434-006-1350-7>, 2006.

815 Pan, B., Pang, H., Gao, H., Garzanti, E., Zou, Y., Liu, X., Li, F., and Jia, Y.: Heavy-mineral analysis and provenance  
816 of Yellow River sediments around the China Loess Plateau, *Journal of Asian Earth Sciences*, 127, 1–11,  
817 <https://doi.org/10.1016/j.jseaes.2016.06.006>, 2016.

818 Qu, Y., Jin, Z., Wang, J., Wang, Y., Xiao, J., Gou, L.-F., Zhang, F., Liu, C.-Y., Gao, Y., Suarez, M. B., and Xu, X.:  
819 The sources and seasonal fluxes of particulate organic carbon in the Yellow River, *Earth Surface Processes and  
820 Landforms*, <https://doi.org/10.1002/esp.4861>, 2020.

821 Ran, L., Lu, X. X., and Xin, Z.: Erosion-induced massive organic carbon burial and carbon emission in the Yellow  
822 River basin, China, *Biogeosciences*, 11, 945–959, <https://doi.org/10.5194/bg-11-945-2014>, 2014.

823 Ran, L., Lu, X. X., Sun, H., Han, J., Li, R., and Zhang, J.: Spatial and seasonal variability of organic carbon transport  
824 in the Yellow River, China, *Journal of Hydrology*, 498, 76–88, <https://doi.org/10.1016/j.jhydrol.2013.06.018>, 2013.

825 Rao, Z., Guo, W., Cao, J., Shi, F., Jiang, H., and Li, C.: Relationship between the stable carbon isotopic composition  
826 of modern plants and surface soils and climate: A global review, *Earth-Science Reviews*, 165, 110–119,  
827 <https://doi.org/10.1016/j.earscirev.2016.12.007>, 2017.

828 Repasch, M., Scheingross, J. S., Hovius, N., Lupker, M., Wittmann, H., Haghypour, N., Gröcke, D. R., Orfeo, O.,  
829 Eglinton, T. I., and Sachse, D.: Fluvial organic carbon cycling regulated by sediment transit time and mineral  
830 protection, *Nat. Geosci.*, 14, 842–848, <https://doi.org/10.1038/s41561-021-00845-7>, 2021.

831 Rouse, H.: Modern Conceptions of the Mechanics of Fluid Turbulence, *Transactions of the American Society of Civil  
832 Engineers*, 102, 463–505, <https://doi.org/10.1061/TACEAT.0004872>, 1937.

833 Schwab, M. S., Hilton, R. G., Haghypour, N., Baronas, J. J., and Eglinton, T. I.: Vegetal Undercurrents—Obscured  
834 Riverine Dynamics of Plant Debris, *Journal of Geophysical Research: Biogeosciences*, 127, e2021JG006726,  
835 <https://doi.org/10.1029/2021JG006726>, 2022.

836 Shi, H. and Shao, M.: Soil and water loss from the Loess Plateau in China, *Journal of Arid Environments*, 45, 9–20,  
837 <https://doi.org/10.1006/jare.1999.0618>, 2000.

838 Stevens, T., Carter, A., Watson, T. P., Vermeesch, P., Andò, S., Bird, A. F., Lu, H., Garzanti, E., Cottam, M. A., and  
839 Sevastjanova, I.: Genetic linkage between the Yellow River, the Mu Us desert and the Chinese Loess Plateau,  
840 *Quaternary Science Reviews*, 78, 355–368, <https://doi.org/10.1016/j.quascirev.2012.11.032>, 2013.

841 Stock BC and Semmens BX. 2016. MixSIAR GUI User Manual. Version  
842 3.1. <https://github.com/brianstock/MixSIAR>. doi:10.5281/zenodo.1209993.

843 Sun, D., Tang, J., He, Y., Liao, W., and Sun, Y.: Sources, distributions, and burial efficiency of terrigenous organic  
844 matter in surface sediments from the Yellow River mouth, northeast China, *Organic Geochemistry*, 118, 89–102,  
845 <https://doi.org/10.1016/j.orggeochem.2017.12.009>, 2018.

846 Syvitski, J. P. M., Vörösmarty, C. J., Kettner, A. J., and Green, P.: Impact of Humans on the Flux of Terrestrial  
847 Sediment to the Global Coastal Ocean, *Science*, 308, 376–380, <https://doi.org/10.1126/science.1109454>, 2005.

848 Tao, S., Eglinton, T. I., Montluçon, D. B., McIntyre, C., and Zhao, M.: Pre-aged soil organic carbon as a major  
849 component of the Yellow River suspended load: Regional significance and global relevance, *Earth and Planetary  
850 Science Letters*, 414, 77–86, <https://doi.org/10.1016/j.epsl.2015.01.004>, 2015.

851 Tao, S., Eglinton, T. I., Montluçon, D. B., McIntyre, C., and Zhao, M.: Diverse origins and pre-depositional histories  
852 of organic matter in contemporary Chinese marginal sea sediments, *Geochimica et Cosmochimica Acta*, 191, 70–88,  
853 <https://doi.org/10.1016/j.gca.2016.07.019>, 2016.

854 Tao, S., Eglinton, T. I., Zhang, L., Yi, Z., Montluçon, D. B., McIntyre, C., Yu, M., and Zhao, M.: Temporal variability  
855 in composition and fluxes of Yellow River particulate organic matter, *Limnology and Oceanography*, 63, S119–S141,  
856 <https://doi.org/10.1002/lno.10727>, 2018.

857 Turowski, J. M., Hilton, R. G., and Sparkes, R.: Decadal carbon discharge by a mountain stream is dominated by  
858 coarse organic matter, *Geology*, 44, 27–30, 2016.

859 Walling, D. E. and Fang, D.: Recent trends in the suspended sediment loads of the world's rivers, *Global and Planetary  
860 Change*, 39, 111–126, [https://doi.org/10.1016/S0921-8181\(03\)00020-1](https://doi.org/10.1016/S0921-8181(03)00020-1), 2003.

861 Wang, C., Li, F., Shi, H., Jin, Z., Sun, X., Zhang, F., Wu, F., and Kan, S.: The significant role of inorganic matters in  
862 preservation and stability of soil organic carbon in the Baoji and Luochuan loess/paleosol profiles, Central China,  
863 *CATENA*, 109, 186–194, <https://doi.org/10.1016/j.catena.2013.04.001>, 2013.

864 Wang, G., Feng, X., Han, J., Zhou, L., Tan, W., and Su, F.: Paleovegetation reconstruction using  $\delta^{13}\text{C}$  of Soil Organic  
865 Matter, *Biogeosciences*, 5, 1325–1337, <https://doi.org/10.5194/bg-5-1325-2008>, 2008.

866 Wang, H., Bi, N., Saito, Y., Wang, Y., Sun, X., Zhang, J., and Yang, Z.: Recent changes in sediment delivery by the  
867 Huanghe (Yellow River) to the sea: Causes and environmental implications in its estuary, *Journal of Hydrology*, 391,  
868 302–313, <https://doi.org/10.1016/j.jhydrol.2010.07.030>, 2010.

869 Wang, H., Wu, X., Bi, N., Li, S., Yuan, P., Wang, A., Syvitski, J. P. M., Saito, Y., Yang, Z., Liu, S., and Nittrouer, J.:  
870 Impacts of the dam-orientated water-sediment regulation scheme on the lower reaches and delta of the Yellow River  
871 (Huanghe): A review, *Global and Planetary Change*, 157, 93–113, <https://doi.org/10.1016/j.gloplacha.2017.08.005>,  
872 2017.

873 Wang, H., Yang, Z., Saito, Y., Liu, J. P., Sun, X., and Wang, Y.: Stepwise decreases of the Huanghe (Yellow River)  
874 sediment load (1950–2005): Impacts of climate change and human activities, *Global and Planetary Change*, 57, 331–  
875 354, <https://doi.org/10.1016/j.gloplacha.2007.01.003>, 2007.

876 Wang, S., Fu, B., Piao, S., Lü, Y., Ciais, P., Feng, X., and Wang, Y.: Reduced sediment transport in the Yellow River  
877 due to anthropogenic changes, *Nature Geosci*, 9, 38–41, <https://doi.org/10.1038/ngeo2602>, 2016.

878 Wang, X., Xu, C., Druffel, E. M., Xue, Y., and Qi, Y.: Two black carbon pools transported by the Changjiang and  
879 Huanghe Rivers in China, *Global Biogeochemical Cycles*, 2016.

880 Weiguo, L., Xiahong, F., Youfeng, N., Qingle, Z., Yunning, C., and Zhisheng, A. N.:  $\delta^{13}\text{C}$  variation of C3 and C4  
881 plants across an Asian monsoon rainfall gradient in arid northwestern China, *Global Change Biology*, 11, 1094–1100,  
882 <https://doi.org/10.1111/j.1365-2486.2005.00969.x>, 2005.

883 Xiubin, H., Tang, K., and Zhang, X.: Soil Erosion Dynamics on the Chinese Loess Plateau in the Last 10,000 Years,  
884 *mred*, 24, 342–347, [https://doi.org/10.1659/0276-4741\(2004\)024\[0342:SEDOTC\]2.0.CO;2](https://doi.org/10.1659/0276-4741(2004)024[0342:SEDOTC]2.0.CO;2), 2004.

885 Xue, D., Lu, J., Leung, L. R., Teng, H., Song, F., Zhou, T., and Zhang, Y.: Robust projection of East Asian summer  
886 monsoon rainfall based on dynamical modes of variability, *Nat Commun*, 14, 3856, [https://doi.org/10.1038/s41467-  
887 023-39460-y](https://doi.org/10.1038/s41467-023-39460-y), 2023.

888 YRCC (Yellow River Conservation Committee): Annual Sediment Report for the Yellow River, 2016.

889 Yu, M., Eglinton, T. I., Haghypour, N., Montluçon, D. B., Wacker, L., Hou, P., Zhang, H., and Zhao, M.: Impacts of  
890 Natural and Human-Induced Hydrological Variability on Particulate Organic Carbon Dynamics in the Yellow River,  
891 *Environ Sci Technol*, 53, 1119–1129, <https://doi.org/10.1021/acs.est.8b04705>, 2019a.

892 Yu, M., Eglinton, T. I., Haghypour, N., Montluçon, D. B., Wacker, L., Wang, Z., Jin, G., and Zhao, M.: Molecular  
893 isotopic insights into hydrodynamic controls on fluvial suspended particulate organic matter transport, *Geochimica et  
894 Cosmochimica Acta*, 262, 78–91, <https://doi.org/10.1016/j.gca.2019.07.040>, 2019b.

895 Zhang, L. J., Wang, L., Cai, W. J., Liu, D. M., and Yu, Z. G.: Impact of human activities on organic carbon transport  
896 in the Yellow River, *Biogeosciences*, 10, 2513–2524, <https://doi.org/10.5194/bg-10-2513-2013>, 2013.

897 Zhu, T. X.: Gully and tunnel erosion in the hilly Loess Plateau region, China, *Geomorphology*, 153–154, 144–155,  
898 <https://doi.org/10.1016/j.geomorph.2012.02.019>, 2012.